Effects of Defocus Distance on Three-Beam Laser Internal Coaxial Wire Cladding

Shaoshan Ji[1], Fan Liu[1], Tuo Shi[2], Geyan Fu[1*] and Shihong Shi[1]

Abstract

Three-beam laser internal coaxial wire feeding cladding is regarded as a promising additive manufacturing technique because it is highly efficient and controllable. In this study, the effects of the defocus distance on cladding using a three-beam laser with internal wire feeding are experimentally and numerically studied. A process map indicating the surface characteristics at different defocus distances with various parameter combinations was developed. The transmission characteristics including laser intensity, beam size, and laser spot distance of the three-beam laser at different defocus distances were analyzed using TracePro software. Based on the TracePro results as heat source, a three-dimensional transient finite element (FE) thermal model was formulated to predict the thermal field, temperature history and molten pool shape at different defocus distances. A molten pool with a flat bottom and low melting depth is generated when the defocus distance is − 2.5 mm, whereas when this distance is − 1.5 mm, a pool with a valley-shaped bond and high melting depth is formed. The simulated results of the temperature cycle and clad geometry are both validated and found to well agree with experimental measurements. The influence of the defocus distance on the microstructure and microhardness are discussed based on the temperature history and cooling rate. With the increase in the absolute defocus distance, the height and dilution of the clad decreased, whereas the width increased. In addition, the effects of defocus distance with various parameter combinations on clad geometry were explored using the formulated FE model.

Keywords: Three beams laser, Wire cladding, Finite element analysis, Defocus distance

1 Introduction

Laser cladding is an additive manufacturing process that uses laser as high-intensity energy source to create a molten pool into which metal powder or wire is injected to build up layers. Compared with conventional welding-based processes, laser cladding affords many advantages; for example, it produces fine grain sizes of deposited materials with low levels of distortion and dilution [1]. In metal manufacturing, laser powder feeding cladding has been widely applied because of its low heat input, high flexibility, and programmable process [2, 3].

As an alternative to powder, the use of wire as feedstock material has significant advantages, such as high material usage efficiency, clean process condition, competitive cost, and low surface roughness [1]. However, between the two, laser wire cladding is more exigent. Currently, the side wire feeding method is predominantly used in the typical laser wire cladding process. In this method, the wire is fed from the side; hence, only half of it can be irradiated by the laser beam. Because of the unbalanced irradiation and heat transfer, the wire can easily bend and jump out of the molten pool, leading to inconsistent processes. The geometry and surface roughness of the cladding layer are also associated with the wire feeding angle, direction, and location [4]. The resulting inconsistencies limit the wide application of laser cladding using filler wire technology [5]. To solve these problems, the wire should be accurately fed into the focused laser spot to

*Correspondence: fugeyan@suda.edu.cn
[1] School of Mechanical and Electrical Engineering, Soochow University, Suzhou 215000, China
Full list of author information is available at the end of the article

Ji *et al. Chin. J. Mech. Eng.* (2021) 34:45

Page 2 of 22

melt the wire and base metal simultaneously [6]. Several studies have been performed to implement wire cladding with a vertically fed wire at the center of the laser. Sandia National Laboratory introduced the concept of using three tilted lasers that converge at a common focal point with the wire in the center. Zhang et al. [7] also developed a coaxial hybrid CO_2-pulsed metal inert gas welding system. However, thus far, these experimental studies have not been practically applied.

Ji and Shi and his co-workers [8] proposed a three-beam laser cladding head with an internal wire delivery system. First, the cladding head splits the input laser beam into three laser beams through a triple prism; then, the three beams focus on the focal plane by three focusing mirrors, as shown in Figure 1. Through this approach, the wire is consistently oriented vertical to the molten pool. The wire is fed at the center of the three laser beams along the axis of the nozzle and evenly irradiated by the beams.

The energy irradiated by the three-beam laser exceeds that of a single laser beam. Ji et al. [9] investigated various approaches to the three-beam laser cladding method (with the wire internally fed) and the resulting characteristics of the clad. A satisfactory clad with single and multiple directions was produced, and the process was considerably easy to control.

Numerical simulation provides a direct and effective way to calculate the thermal field and the evolution of the molten pool boundary which affect the metallurgical bonding between the cladding material and substrate [10–12]. The numerical models were experimentally verified after implementing certain simplifications. The performed numerical works is helpful to understand the physical mechanisms of laser cladding. Based on mass and energy balance, Wei et al. [13] developed a two-dimensional thermal model incorporating the powder efficiency and solved it using the finite element (FE) software COMSOL MULTIPHYSICS. Parisa et al. [14] presented a three-dimensional (3D) transient uncoupled thermoelastic–plastic model to simulate the thermal process and subsequently thermally induced the residual stress in laser cladding. Hao et al. [15] built a 3D thermal FE model using an inverse modeling approach to simulate the temperature field in Ti6Al4V (TC4) cladding.

Some studies have determined the relationships between the process inputs and final track characteristics. Most of these studies, which are based on experiments and theoretical modeling, are mainly concentrated on certain parameters, such as laser power, powder mass, flow rate, and scanning speed using regression methods [16–19]. Abioye et al. [20] developed a process map to predict the process characteristics under different cladding conditions used for Inconel 625 wire laser deposition. Keeping the power and travel speed constant, Toyserkani et al. [21] found that the molten pool depth decreased with the increase in the powder feed rate. Toyserkani et al. [1] found that both the pool depth and dilution were directly and inversely related to the linear heat input and travel speed, respectively. Tabernero et al. [22] investigated the effects of laser attenuation and power distribution on the cladding geometry. Liu et al. [23] discovered that the geometrical characteristics of the sectional profile of single clad could be described as a circular arc, and the sectional profile could be predicted based on the input parameters. Riquelme et al. [24] investigated the effects of laser power, scanning speed, and
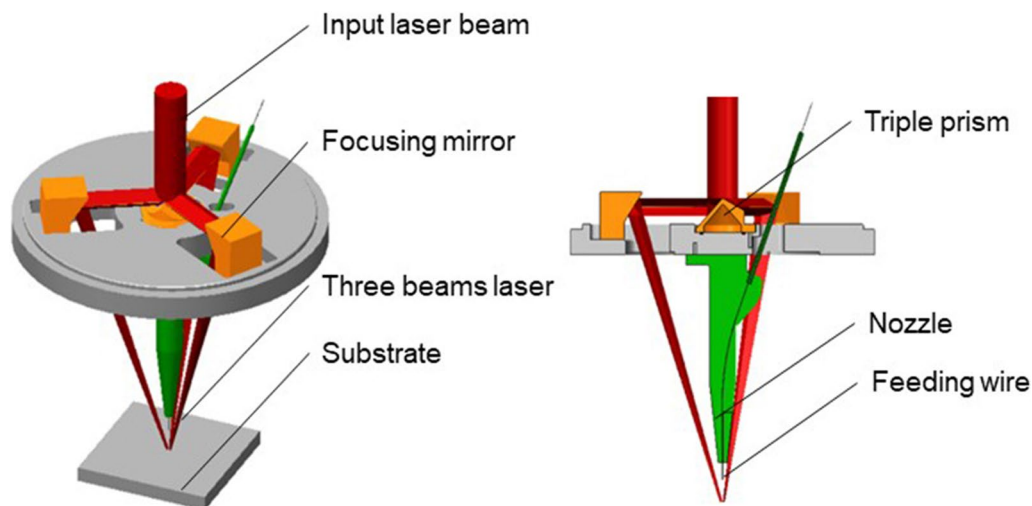
Figure 1 Schematics of three-beam laser with internal coaxial wire feeding cladding head [9]

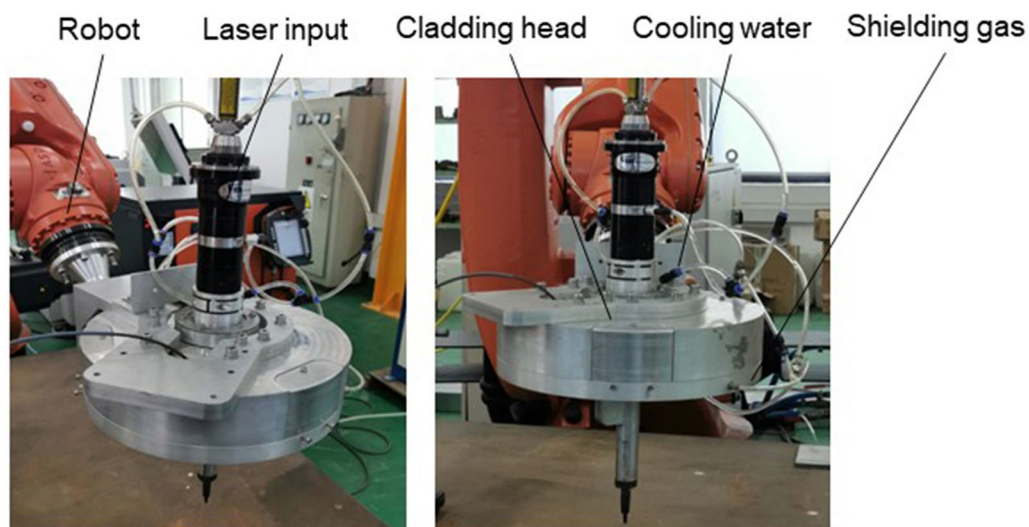Ji *et al. Chin. J. Mech. Eng.*   (2021) 34:45

Page 3 of 22

powder feeding rate on the dilution and clad geometry in Al–SiCp laser cladding. Zhu et al. [25] also suggested that the energy intensity reaching the molten pool was dependent on the laser power and scanning velocity.

As an important cladding parameter, the defocus distance has significant effects on laser beam dimension and laser intensity distribution. A positive defocus is defined as the work plane below the focal plane of the laser beam. Conversely, a negative defocus indicates that the work plane is above the focal plane of the laser beam. Gao et al. [26] found that a negative defocus was effective in solving the problems of high dilution rate and pores in powder coating by comparing the samples of positive focus and negative focus using a Gaussian laser beam. Most of the studies simply set the defocus distance as a constant parameter; for example, a negative defocus of -3 mm [27] was used based on experience. The influence of process inputs on the dilution and geometry of the clad can be attributed to the change in the distribution of energy absorbed by the cladding layer and substrate. Varying the defocus distance in the cladding process does not only change the laser beam dimension but also the laser intensity distribution, considerably affecting the cladding characteristics. Although many of the previous works have focused on the relationships between the clad characteristics and process parameters (e.g., laser power, flow rate, and traverse speed), insight into the governing impact of defocus distance on laser cladding, especially on the wire feeding method, is minimal. Furthermore, no work had ever focused on the influence of the defocus distance on cladding using a three-beam laser with internal wire feeding.

In this study, the effects of the defocus distance on cladding using a three-beam laser with internal coaxial wire feeding are experimentally and numerically studied. The transmission characteristics of the three-beam laser at different defocus distances, including the energy intensity, beam size, and laser spot distance, were calculated using TracePro software. A process map indicating the surface quality at different defocus distances with various parameter combinations was developed. A 3D FE thermal model based on the TracePro results was formulated to simulate the variations in the thermal process and clad geometry at different defocus distances. The predictions of the thermal model were validated by measurements using an infrared thermometer and the comparison between the experimental and predicted cross-sections of the clad. The predicted clad geometries were compared with experimental measurements. The resulting microstructure and microhardness of the clad at different defocus distances were also investigated. Finally, the effects of the defocus distance with different parameter combinations on the clad geometry are discussed.

2 Experimental Procedures

The three-beam laser cladding head with an internal wire feeding system employed in the experiments are shown in Figure 2. Cladding was performed using an IPG YLS-2000-TR fiber laser with a maximum power of 2 kW. The three-beam laser cladding head with an internal wire feeding system vertically delivered the wire to the molten pool; it also protected the wire by coaxially applying a protective gas. In addition to shielding the wire and molten pool from oxidation, the gas also protected the

Figure 2 Cladding experimental setup [9]

Ji *et al. Chin. J. Mech. Eng.* (2021) 34:45

Page 4 of 22

laser optics from contamination. An M322-type infrared thermometer with a test range of 800–3000 °C was used to measure the temperature. Further details on the three-beam laser cladding system can be found in Ji et al. [9].

A 150 mm × 150 mm × 10 mm stainless steel #304 plate was used as the substrate material. The wire employed as feeding material was stainless steel #304 with a diameter of 0.8 mm. The substrate was polished, cleaned with acetone or alcohol, and dried before cladding. The chemical composition of stainless steel #304 is summarized in Table 1.

Based on experimental trials, when the three-beam laser coaxial wire cladding is used with positive defocus, the wire was rapidly overheated by the irradiating beams and formed drops before reaching the molten pool. Hence, this paper mainly discusses negative defocus and its calculation. The experimental process parameters are summarized in Table 2. A total of 135 combinations were performed for the given parameters to build the process map according to the resulting surface characteristics.

Smooth tracks were chosen for the geometrical and microstructural studies as well as the validation of the thermal FE model. The smooth cladding layers were perpendicularly sectioned across the cladding direction by electrical discharge machining; subsequently, each specimen cross-section was polished and etched. The clad geometry and microstructure were investigated, and the geometric characteristics were examined using optical

microscopy. Hardness was checked using a microhardness tester, and the microstructure was investigated by scanning electron microscopy.

3 Numerical Modeling

A 3D thermal FE model was developed to simulate the temperature evolution and molten pool shape during the cladding process. The three-beam laser transmission characteristics, including the laser intensity distribution, beam size, and laser spot distance calculated by Trace-Pro, were used for the input heat load. In this study, to achieve a feasible FE simulation, the following simplifying assumptions are made because of the complexity of the cladding process. Note that their effect on the results is negligible.

- The cladding and substrate materials are isotropic.
- The chemical reactions and stir convection in the molten pool liquid metal are negligible.
- Inert gas flow may be ignored.

3.1 Thermal Model

The thermal analysis is based on the density (ρ), thermal conductivity (k), and specific heat (C_P), which are temperature-dependent (Table 3). The governing thermal equilibrium equation is expressed as [29]

Table 1 Chemical composition of stainless steel #304

Composition	C	Si	Mn	Cr	P	Ni	S	Fe
Mass ratio (%)	≤ 0.07	≤ 1.0	≤ 2.0	17.0–19.0	≤ 0.035	8.0–11.0	≤ 0.03	Bal.

Table 2 Process parameters

Parameters	Value					Unit
Defocus distance	-0.5	-1.5	-2	-2.5	-3.5	mm
Laser power	1.1	1.3	1.5			kW
Scanning speed	4	6	8			mm/s
Wire feeding speed	17.5	20.5	23.5			mm/s

Table 3 Properties of stainless steel #304 [28]

T (℃)	25	200	400	600	800	1000	1200	1400	1454	1600	1800
ρ (kg/m³)	8020	7950	7860	7750	7645	7530	7430	7300	6900	6780	6615
C_p (J/kg·℃)	500	535		616		696		776			856
K (W/m·℃)	14.85	18.41	22.41	26	30.41	34.41	38.41	42.41		46.41	50.41
L (J/g)	265.2										

Ji *et al. Chin. J. Mech. Eng.*   (2021) 34:45

Page 5 of 22

$$\frac{\partial\left(\rho c_{\mathrm{p}}T\right)}{\partial t} = \nabla(k\nabla T) + Q, \tag{1}$$

where T is the temperature, t is time, and Q is the heat generation rate. To solve the thermal equilibrium equation, the boundary and initial conditions must be defined.

The initial condition is defined as

$$T\left(x, y, z, 0\right) = T_0 \quad \text{for} \quad (x, y, z) \in D,$$

where D is the heat source moving domain, and T_0 is the measured ambient temperature.

The essential boundary condition is described as

$$T(x, 0, z,) = T_0 \quad \text{for} \quad (x, z) \in S_1 \quad \text{and} \quad t > 0,$$

where S_1 is the bottom surface of the substrate.

The remaining surfaces of the model were considered to be subjected to convection, radiation, and imposed heat flux. The natural boundary condition can be defined as [30]

$$k_n \frac{\partial T}{\partial n} - q + h(T - T_0) + \sigma\varepsilon\left(T^4 - T_0^4\right) = 0, \tag{2}$$

where T and T_0 are the surface and ambient temperatures, respectively; ε is the emissivity of the material; and σ is the Stephen–Boltzmann constant for radiation. Convection and radiation can be summed to a single heat transfer coefficient and integrated into the FE analysis. In this model, heat transfer coefficients of 120 and 40 $\mathrm{W/m^2 \cdot {}^\circ C}$ were applied to the bottom surface and sides, respectively [28, 30].

3.2 Geometric Model
In checking the clad micrograph (Figure 3(a)), the transverse cross-section of the cladding layers is noted to be considerably similar to a circular arc. The geometrical features of a circular arc can be approximately defined by the clad width (w), height (h), and arc radius (R), as

shown in Figure 3(b). Therefore, the geometrical definition of the clad is expressed as

$$\begin{cases} y = \left(\frac{h}{2} + \frac{w^2}{8h}\right)\cos\left(\frac{\theta_2 - \theta_1}{2}\right) 0 \le \theta_1 \le \frac{\pi}{2} - \arcsin\left(\frac{4hw}{w^2 + 4h^2}\right), \\ z = \left(\frac{h}{2} + \frac{w^2}{8h}\right)\sin\left(\frac{\theta_2 - \theta_1}{2}\right) \frac{\pi}{2} \le \theta_1 \le \frac{\pi}{2} + \arcsin\left(\frac{4hw}{w^2 + 4h^2}\right). \end{cases} \tag{3}$$

where the clad width (w) and height (h) are obtained from the optimization of the geometric characteristics of the model given in Eq. (4) [31]. As a result, the clad geometry can be accurately predicted by the FE model at different process parameter combinations without further experimentation.

$$\begin{cases} w = \sqrt{\frac{2((1-\eta_1)\eta_2\eta_3 P)}{V_S\rho_{\mathrm{m}}\left(C_P\left(T_f - T_0\right) + L\right)} - h^2} + (R_1 + R_2)(1 - \alpha V_S), \\ h = R - \sqrt{R^2 - \left(\frac{w}{2}\right)^2}, \\ \frac{\pi r^2 V_f}{V_s} = R^2\arcsin\frac{w}{2R} - \frac{w}{2}\sqrt{R^2 - \left(\frac{w}{2}\right)^2}, \end{cases} \tag{4}$$

where P is the laser power; V_s is the scanning velocity; V_f is the wire feeding speed; r is the wire radius; C_P is the temperature-dependent specific heat; L is the latent heat; T_f is the steady temperature; R_1 is the radius of each beam; R_2 is the laser spot distance radius; and α is the coefficient whose selected value is based on experience.

Dilution is defined as follows [21]:

$$\lambda = \frac{b}{h + b}, \tag{5}$$

where b is the molten pool depth measured from the top surface of the substrate to the bottom of the boundary of the original substrate and cladding area, as shown in Figure 3(a).
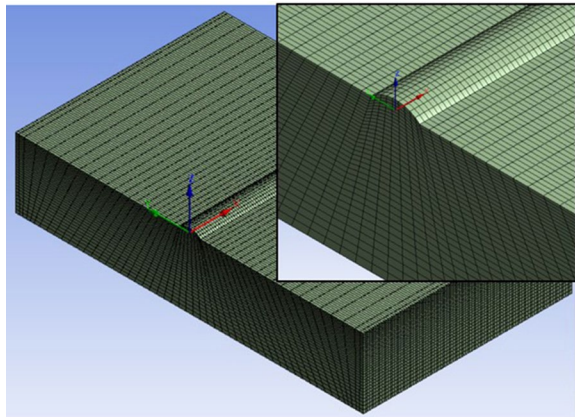
3.3 Numerical Implementation by ANSYS
The geometry and 3D mesh employed for the thermal analysis are shown in Figure 4. Owing to the high thermal gradient during the laser cladding process, the closer the
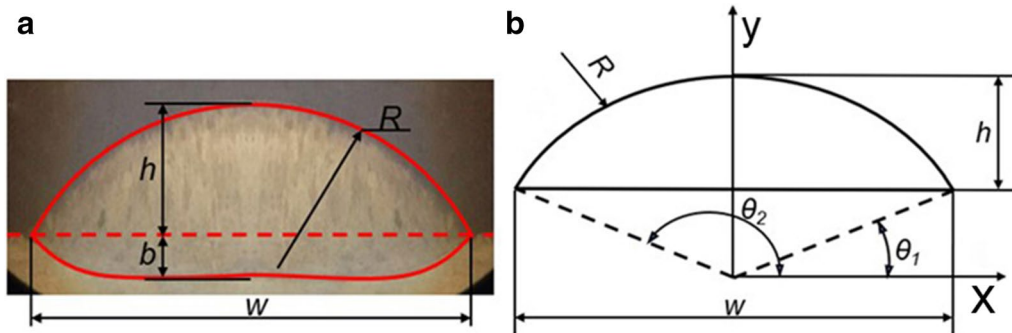
Figure 3 Geometrical characteristics of clad: **a** micrograph and **b** geometric model of cladding track

Ji *et al. Chin. J. Mech. Eng.   (2021) 34:45
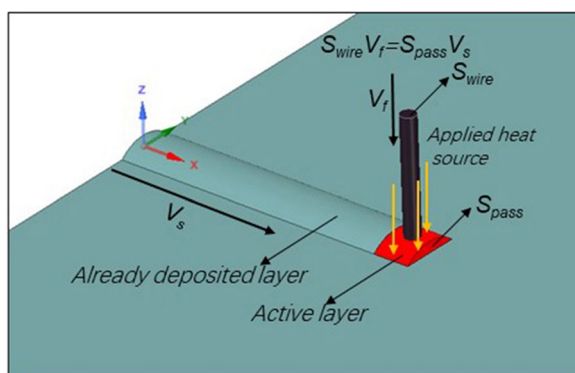
Page 6 of 22

Figure 4 FE mesh

area to the clad zone, the finer the mesh adopted. The fine element size is 0.3 mm in the clad zone. A coarse mesh with an element edge size of up to 2 mm was adopted in the substrate far from the clad zone.

The energy used to melt the wire mainly emanates from the heat conduction of the molten pool and radiation of the three-beam laser. However, note that the three-beam laser is actually the only energy source because it is the sole heat source. As the wire melts and is fed into the molten pool, its energy is also transmitted into the pool. In this study, to simplify the calculation and satisfy the conservation of the total heat input, the three-beam laser is assumed to be mainly applied to the molten pool, and the thermal profile of the feeding wire is neglected. As a simplification, the process by which the wire melts into the molten pool to form the cladding layer is considered as a material accumulation process along the scanning direction, as shown in Figure 5. The technology of element birth and death was utilized to simulate the material addition in the cladding process. According

to the mass conservation law, the molten wire builds an equal mass of the cladding layer. It can also be expressed by multiplying the cross-sectional area of the cladding layer (S_{pass}) and scanning speed (V_S). The product is equal to that obtained by multiplying the cross-sectional area (S_{wire}) and feeding speed (V_f) of the wire. At the beginning of the process, all cladding layer elements are defined; however, they are rendered inactive by the application of the reduction factor. This means that the inactive elements contribute a near-zero conductivity value to the overall thermal model. When heat loads are applied to the laser-scanned region with the movement of the heat source, the reduction factor is removed, and the elements are gradually activated. Similar methods have been adopted by the laser wire cladding numerical models; the simulation results well agree with the experimental results [32, 33].

4 Heat Source
4.1 Simulation Implementation by TracePro
To describe the cross-section of the energy distribution of the three-beam laser at different defocus distances, the transmission characteristics of the laser beam through the triple prism and three paraboloidal mirrors were simulated by TracePro. A schematic of the three-beam laser transmission is shown in Figure 6. The cylindrical laser beam through a collimator lens is then split by a triple prism into three laser beams, which are focused by three paraboloidal mirrors at the focal plane. These mirrors are described by the following [9]:

Figure 5 Technology of element birth and death
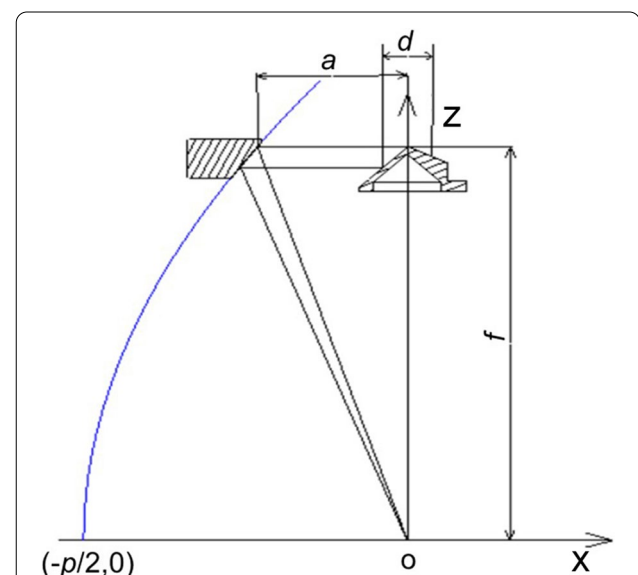
Figure 6 Schematics of transmission of three-beam laser [9]

Ji *et al. Chin. J. Mech. Eng.*   (2021) 34:45

Page 7 of 22

$$y^2 + z^2 = 2\left(a + \sqrt{a^2 + f^2}\right)\left(x + \frac{a + \sqrt{a^2 + f^2}}{2}\right),$$
(6)

where x, y, and z are the local coordinates; a is the distance from the vertex of the triple prism to the focal lens; O is the focus on the three beams; and f is the vertical distance between focus O and the vertex of the triple prism. To avoid interference between the laser beam and wire, the volume of the nozzle was defined with level and vertical distances of $a = 95$ mm and $f = 300$ mm, respectively.

The 3D model of the lens system (Figure 7) created using Creo software was implemented in TracePro to simulate the laser transfer system. The input laser was assumed to have a Gaussian distribution. The absorption coefficient of the lens system, including the triple prism and focusing lenses, is denoted as η_1. The absorption coefficient of the substrate and cladding material is indicated as η_2. Further details on the TracePro simulation can be found in Ji et al. [9].

4.2 Input Heat Model
The Gaussian model is employed to describe the heat source:

$$q(r) = q_m \exp\left(-\frac{3r^2}{R_1^2}\right),$$
(7)
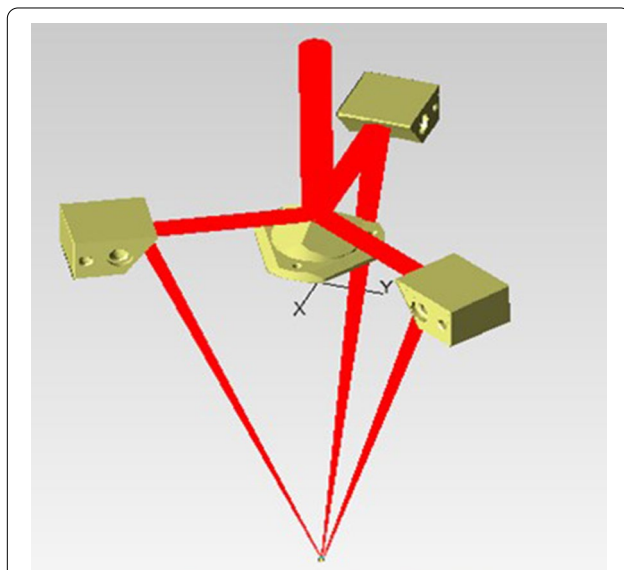
Figure 7 3D model of lens system and transmission of three-beam laser [9]

where R_1 is the radius of the laser beam, r is the radical distance from the center of the laser beam, and q_m is the maximum power intensity.

5 Results and Discussions
5.1 Transmission Characteristic of Three-Beam Laser
The transmission characteristic of the laser beam through the triple prism and three paraboloidal mirrors simulated by TracePro is shown in Figure 8(a). Through the triple prism, the cylindrical solid laser beam is evenly split into three beams. The wire is located in the center and the beams are focused by the paraboloidal mirrors to a circular focal point at the focus plane. The three-dimensional images of beam distribution on the negative focus, focal, and positive focus planes, are illustrated in Figure 8(b)–(d), respectively. With the decrease in the absolute defocus distance, the diameter of each laser beam decreases and the three beams merge toward the focus. With their uniform diameter, the three beams could be assumed to have an identical energy distribution following a Gaussian distribution.

The contour image of laser power intensity and dimension of the laser beams at the negative defocus cross-section are shown in Figure 9. The global laser beam concentration intensity, $q(r)$, is calculated by adding the Gaussian intensity functions of the laser beam from the three-beam laser in the (x, y) coordinate system. The energy intensity of each laser beam is first determined in their local axis before a global coordinate transformation is applied. The laser power intensity of each laser beam is given by

$$q(r_n) = q_m \exp\left(-\frac{3r_n^2}{R_1^2}\right),$$
(8)

where $r_n^2 = x_n^2 + y_n^2$ and $n = 1, 2, 3$ (here, x_n and y_n refer to the corresponding local coordinate axes of laser beams 1–3); R_1 is the laser beam radius; and q_m is the maximum power intensity. The local coordinate systems expressed in terms of global coordinate system are as follows:

Laser beam 1 (centerO_1) : $x_1 = x + R_2 \sin 30°$, $y_1 = y - R_2 \cos 30°$.
Laser beam 2 (centerO_2) : $x_2 = x + R_2 \sin 30°$, $y_2 = y + R_2 \cos 30°$.

Laser beam 3 (centerO_3) : $x_3 = x - R_2$, $y_3 = y$. (9)

The energy intensity distribution in the negative defocus cross-section is described as follows:

Ji et al. Chin. J. Mech. Eng.   (2021) 34:45

Page 8 of 22
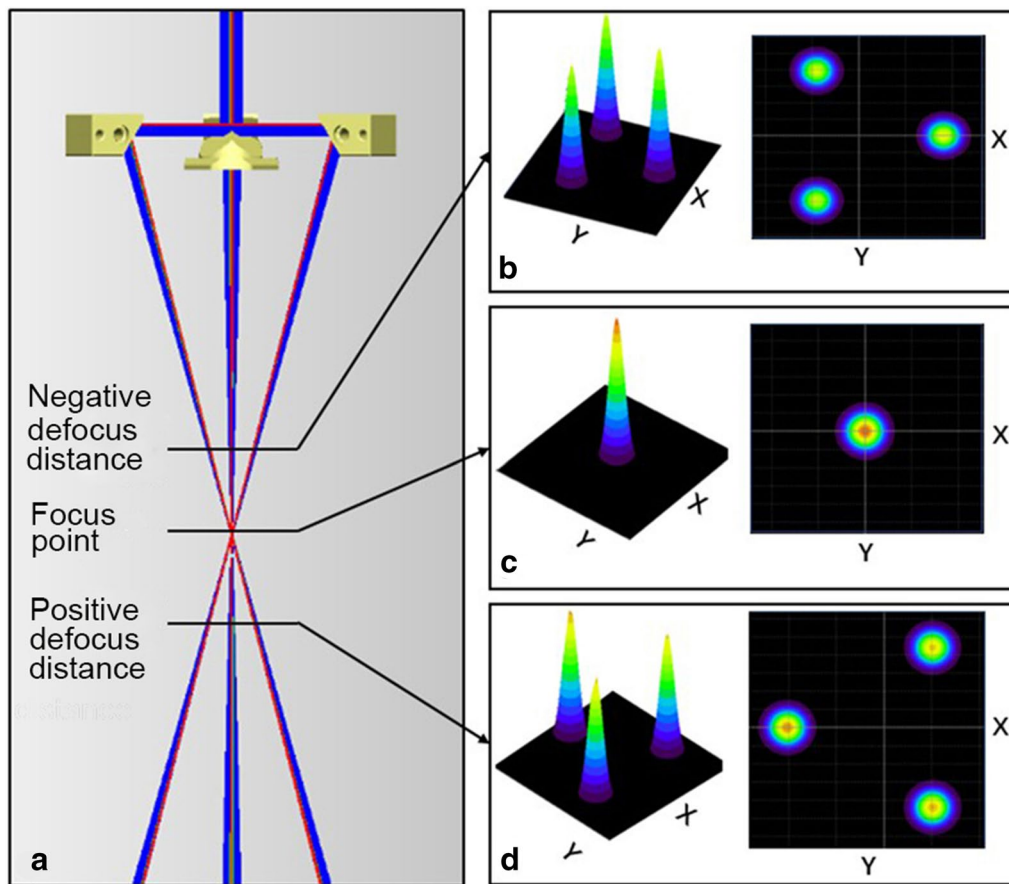
Figure 8 Schematic of three-beam laser simulated by TracePro: **a** transmission characteristic, **b** beams at negative defocus, **c** beams at focal plane, and **d** beams at positive defocus
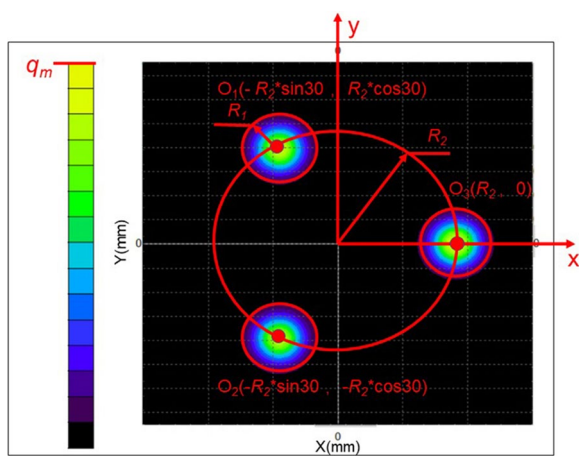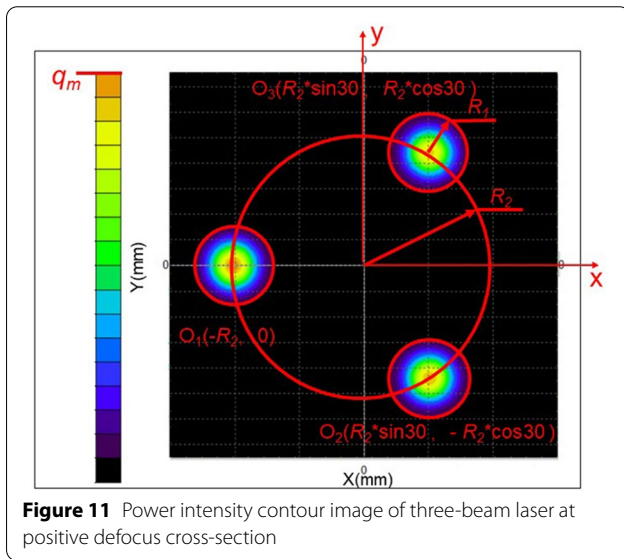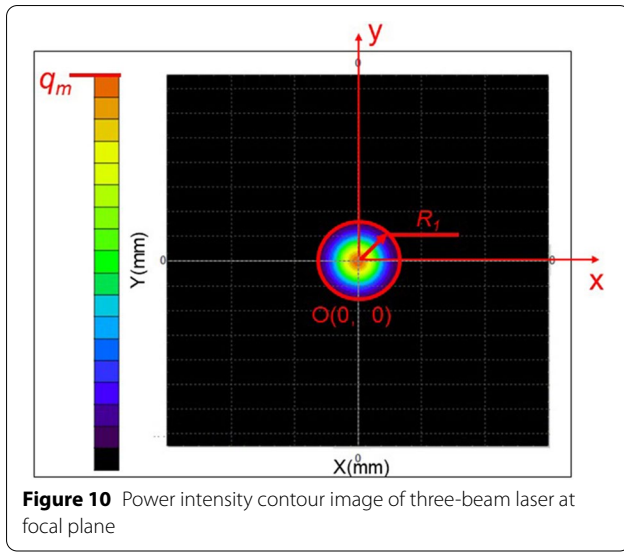

Figure 9 Power intensity contour image of three-beam laser at negative defocus cross-section

$$q(r) = q_m \exp\left(-\frac{3\left((x + R_2 \sin 30°)^2 + (y - R_2 \cos 30°)^2\right)}{R_1^2}\right)$$

$$+ q_m \exp\left(-\frac{3\left((x + R_2 \sin 30°)^2 + (y + R_2 \cos 30°)^2\right)}{R_1^2}\right)$$

$$+ q_m \exp\left(-\frac{3\left((x - R_2)^2 + y^2\right)}{R_1^2}\right).$$

(10)

where R_1 is the radius of each laser beam; R_2 is the radius of the circle formed by the centers of the three beams; q_m is the maximum power intensity. Variables x and y are the coordinates. The points $O_1(-R_2 \sin 30°, R_2 \cos 30°)$, $O_2(-R_2 \sin 30°, -R_2 \cos 30°)$, and $O_3(R_2, 0)$ define the central positions of the three laser beams.

Ji *et al. Chin. J. Mech. Eng.* (2021) 34:45

Page 9 of 22

Figure 10 Power intensity contour image of three-beam laser at focal plane

Figure 11 Power intensity contour image of three-beam laser at positive defocus cross-section

A contour image of the laser power intensity at the focal plane where the three beams merge is shown in Figure 10. The power intensity distribution at the focal plane is expressed as follows:

$$q(r) = q_m \exp\left(-\frac{3(x^2 + y^2)}{R_1^2} \right). \tag{11}$$

The contour image of the power intensity and dimension of the laser beam at the positive cross-section is shown in Figure 11. The power intensity distribution in the positive region is expressed as follows:

Figure 12 Power intensity and three-beam laser dimensions at various defocus distances calculated by TracePro
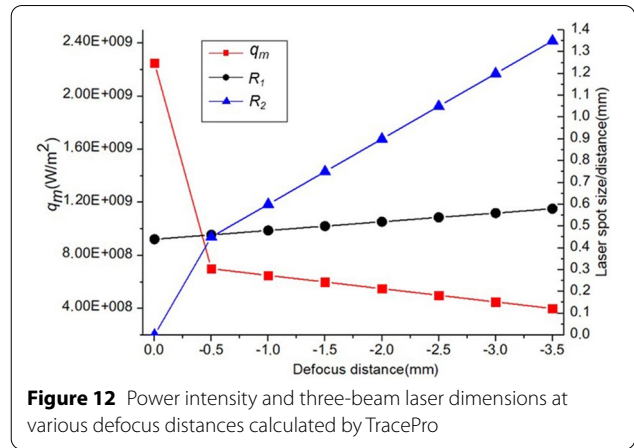
$$
\begin{aligned}
q(r) = {} & q_m \exp\left(-\frac{3\left((x - R_2 \sin 30°)^2 + (y - R_2 \cos 30°)^2\right)}{R_1^2} \right) \\
& + q_m \exp\left(-\frac{3\left((x - R_2 \sin 30°)^2 + (y + R_2 \cos 30°)^2\right)}{R_1^2} \right) \\
& + q_m \exp\left(-\frac{3\left((x + R_2)^2 + y^2\right)}{R_1^2} \right)
\end{aligned}
\tag{12}
$$

At different defocus distances, the three-beam laser's characteristics, such as maximum power intensity (q_m), radius of each laser beam (R_1), and radius of the circle formed by the centers of the three beams (R_2), were calculated using TracePro. The laser spot distance was expressed as $2R_2$. The calculated results at the negative defocus distance from 0 to -3.5 mm are presented in Figure 12. The dimensions of each beam and laser spot distance increased; however, the power intensity (q_m) considerably decreased with an increase in the absolute defocus distance. The three beam spots merge rapidly as the absolute defocus distance decreases. A small absolute defocus distance evidently results in high power intensity and small laser spot size with a short distance.

5.2 Surface Characteristics of Clad at Different Defocus Distances with Various Parameter Combinations

A process map based on the experiments listed in Table 2 at defocus distances ranging from -0.5 mm to -3.5 mm with various parameter combinations is shown in Figure 13. Different surface characteristics are generated by various combinations of the defocus distance with laser power, scanning speed, and wire feeding speed. In the process map, regions 1–5 representing the observed characteristics including dripping, possible dripping,

Ji *et al. Chin. J. Mech. Eng.*   (2021) 34:45

Page 10 of 22
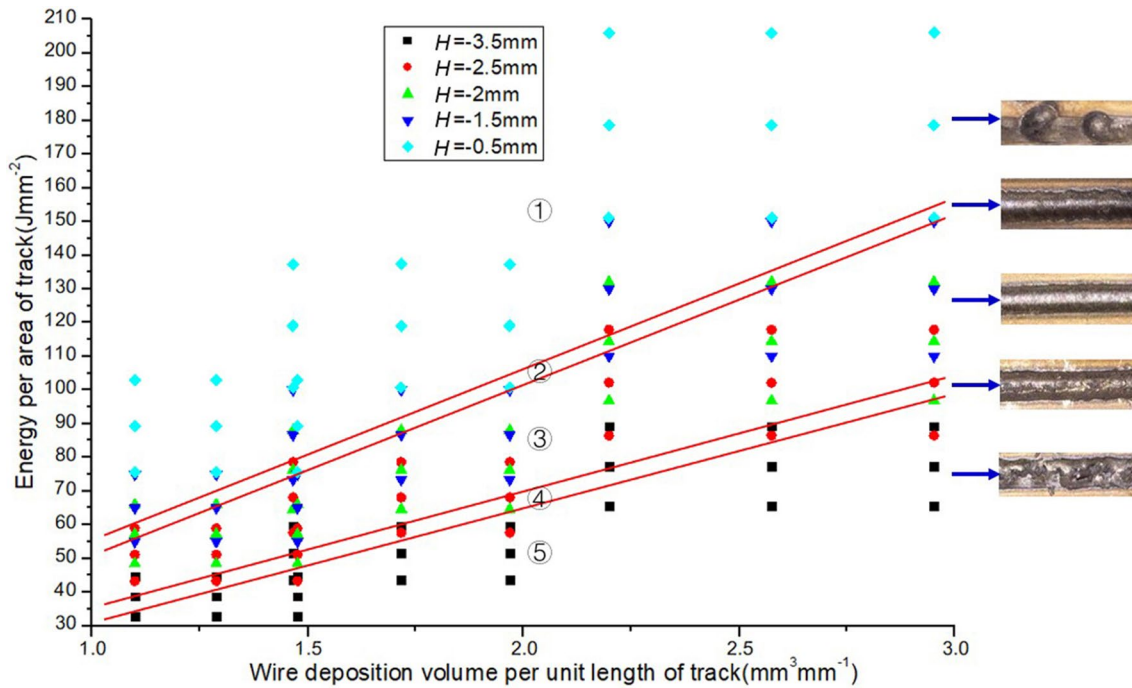
Figure 13 Process map for three-beam laser with internal wire deposition characteristics at different defocus distances with various parameter combinations

smooth surface, possible stubbing, and stubbing are defined, respectively. Typical examples of the clad surface characteristics in the five regions are also presented in Figure 13.

The energy per unit area (E_L) on the *y*-axis of the map is expressed as

$$E_L = \frac{P}{2(R_1 + R_2)V_S},$$ (13)

where P is the laser power, V_S is the scanning speed. $2(R_1 + R_2)$ is the outer diameter of the circle formed by the three beams, and positively dependent on the defocus distance (Figure 12).

The deposition volume per unit length of the clad (D_{VL}) on the *x*-axis of the map is defined as

$$D_{VL} = \frac{\pi r^2 V_f}{V_S},$$ (14)

where r is the wire radius, and V_f is the wire feeding speed.

As defined in Eq. (13), the energy per unit area (E_L) increases with the laser power but decreases with increasing defocus distance and scanning speed. Based on Eq. (14), the deposition volume per unit length could be increased by either decreasing the scanning speed (V_S) or increasing the wire feeding speed (V_f). Owing to the

high energy caused by the low defocus distance or high laser power, the wire tip excessively fuses and gets out the touch of the molten pool. Thus, intermittent dripping occurs resulting in a discontinuous clad with spatters and a burnt surface, as shown in region 1 in Figure 13. A similar result was observed when the wire deposition volume per unit length was excessively low for a fixed amount of energy per unit area. In contrast, stubbing is observed when the defocus distance is high or the energy per unit area is low for a fixed wire deposition volume per unit length, as shown in area 5 in Figure 13. Because the energy is extremely low to melt the wire in time for the given deposition volume per unit length, the unmelted wire leads to stubbing. The same result was generated by the excessive deposition volume per unit length for the given energy per unit area. The boundary between the dripping and smooth regions is in region 2. Region 4 is the boundary between the stubbing and smooth regions. Smooth cladding layers with acceptable dimensions were generated by the parameter combinations in region 3 in the process map.
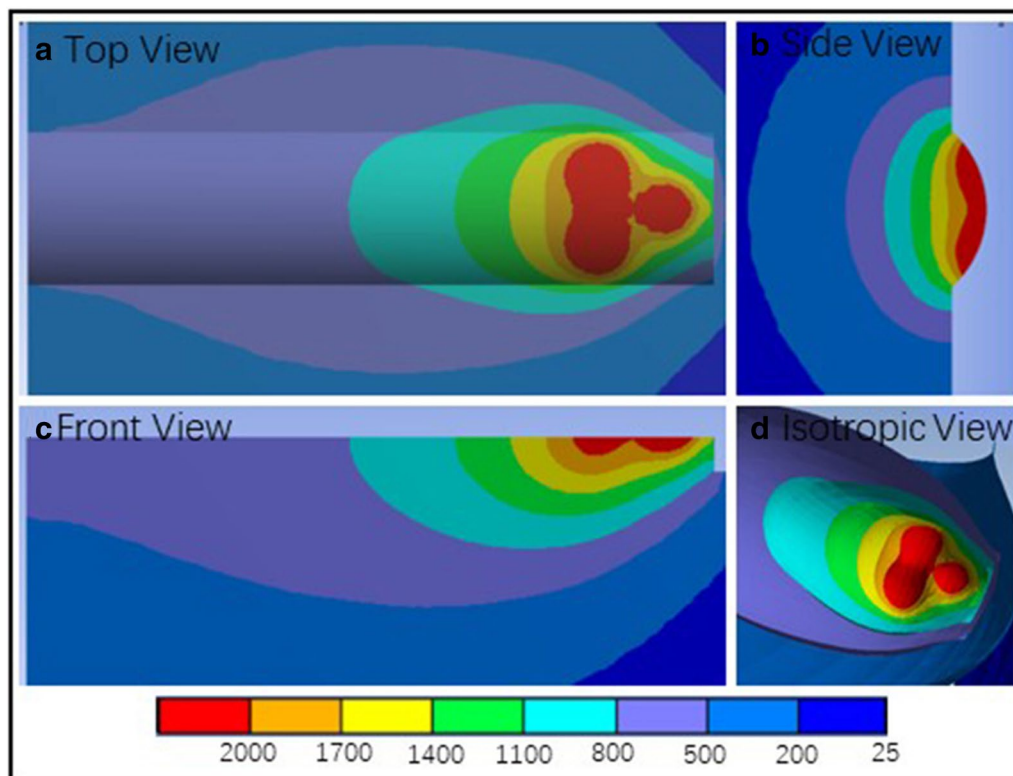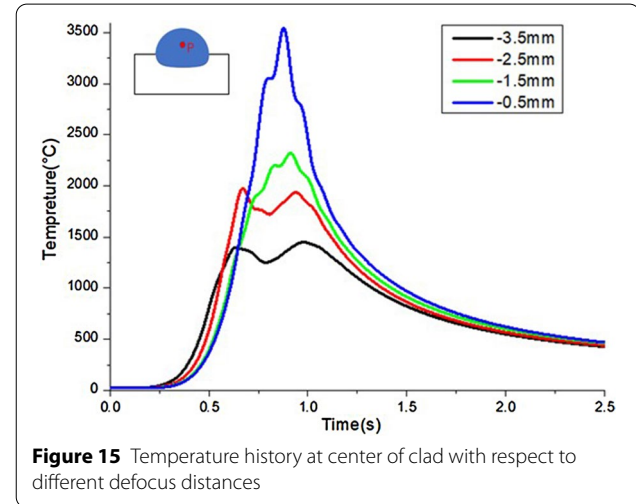
As the defocus distance increases in the process map, the cladding layer surface transitions from cladding with wire dripping to a smooth surface and then cladding with wire stubbing. This shows that cladding with wire dripping can be eliminated by either enhancing the defocus distance (i.e., reducing the energy intensity), *H*,

Ji *et al. Chin. J. Mech. Eng.* (2021) 34:45

Page 11 of 22

from -1.5 to -2.5 mm or reducing the laser power. In addition, wire stubbing can be eliminated by either increasing the energy intensity (i.e., decreasing the defocus distance or increasing the laser power) or decreasing the deposition volume per unit length.

Most of the smooth cladding layers in region 3 are obtained when the defocus distance is from -1.5 to -2.5 mm with the proper beam size and energy intensity. Owing to the small beam size and high energy intensity at $H = -0.5$ mm, the wire overheats and melts outside the molten pool. Thus, a discontinuous clad layer with spatters and a burnt surface is predominant at a low defocus distance, as shown in region 1 in the process map. At a defocus distance of -3.5 mm, the resulting large beam size has low energy intensity and is insufficient to melt the wire in time to achieve the deposition volume. Consequently, the wire tip touches the bottom of the molten pool. Therefore, at a defocus distance of -3.5 mm, wire stubbing resulting in fragmented and warped cladding layers is predominant, as shown in region 5. The thermal cycle at different defocus distances leading to various surface characteristics are further discussed in Section 5.3.

5.3 Temperature Evolution

The FE model employs the results calculated by TracePro (Section 5.1). These results include the energy intensity distribution, laser beam size, and laser spot distance as input heat loads at different defocus distances in the thermal analysis.

Figure 15 Temperature history at center of clad with respect to different defocus distances

Figure 14 Temperature contour images: **a** top view, **b** side view, **c** front view, and **d** isotropic view

Ji *et al. Chin. J. Mech. Eng.* (2021) 34:45

Page 12 of 22

The temperature contour isothermal distribution in the laser cladding at $H = -2.5$ mm with the laser power of 1300 W, scanning speed of 6 mm/s, and wire feeding rate of 20.5 mm/s ($E_L = 68.1$ J/mm^2; $D_{VL} = 1.72$ mm^3/mm in the process map in Figure 13) is shown in Figure 14. The area with the highest temperature is formed by three similar circles merging in the molten pool, as shown in the top view. The temperature distribution well agrees with the power intensity distribution simulated by Trace-Pro. A steeper temperature gradient on the front side of the molten pool than that on the rear side was observed. A further investigation of the temperature shows that the heat input near the edge of the track is enhanced by the three-beam laser from the side. The side and front views indicate that the temperature at the center of the molten pool is effectively alleviated. A heart-shaped molten pool area is observed from the isotropic view.

The history of temperature at the center of the clad at different defocus distances with laser power of 1300 W, scanning speed of 6 mm/s, and wire feeding rate of 20.5 mm/s ($E_L = 51.6$ J/mm^2, 68.1 J/mm^2, 86.7J/mm^2 and $D_{VL} = 1.72$ mm^3/mm in the process map in Figure 13) is shown in Figure 15. The maximum temperature and temperature evolutions differ and depend on the defocus distance. The maximum temperature significantly decreases with the increase in the absolute defocus distance due to the decrease in power intensity with the increase in each beam size ($2R_1$) and laser spot distance ($2R_2$) (Figure 12). When the defocus distance is decreased to -0.5 mm, the laser spot distance is extremely small that it can be assumed as a single Gaussian beam formed by the overlapping of three beams. Hence, the temperature virtually follows a Gaussian profile characterized by one peak value at the center when the defocus distance is -0.5 mm.

Figure 16 Molten pool shapes at various defocus distances: **a** $H = -3.5$ mm, **b** $H = 2.5$ mm, **c** $H = -1.5$ mm, and **d** $H = -0.5$ mm

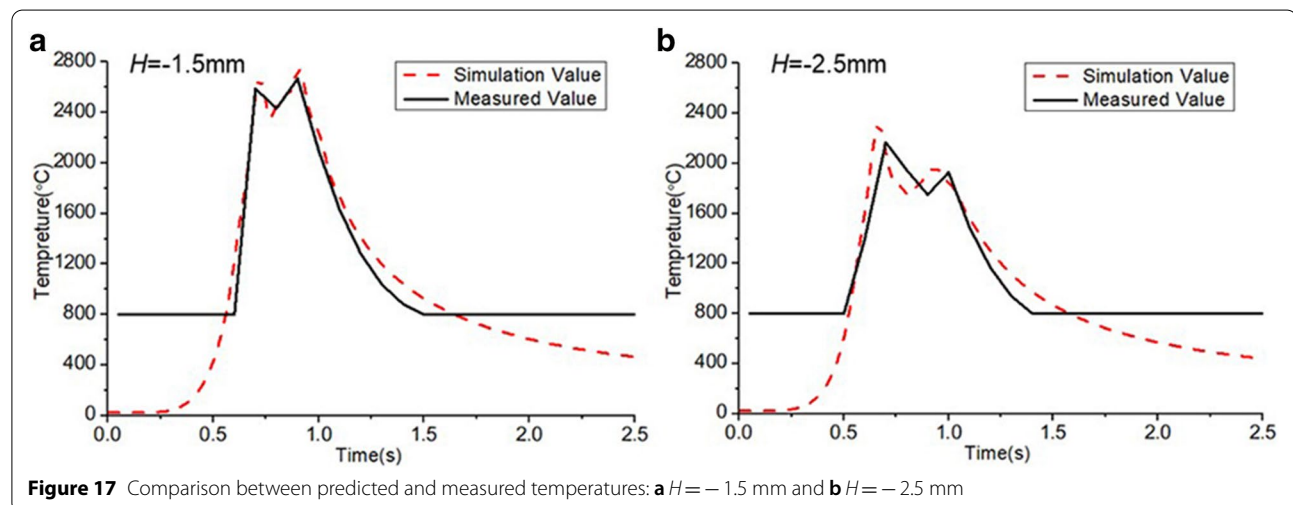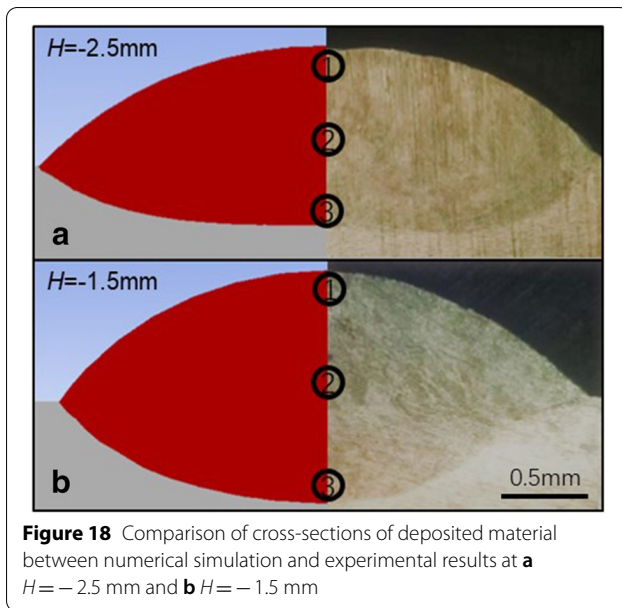Ji *et al. Chin. J. Mech. Eng.*   (2021) 34:45

Page 13 of 22
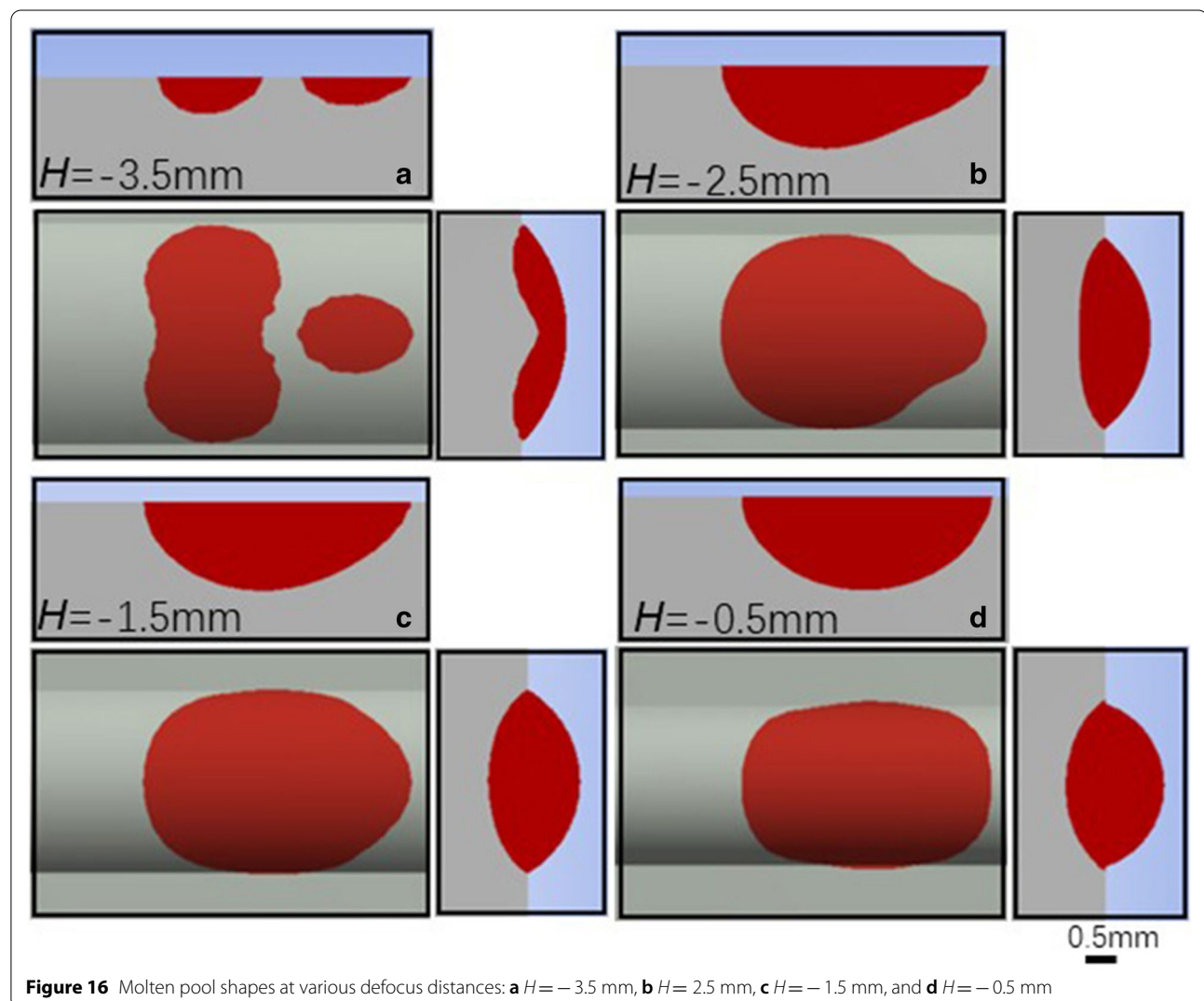
An M-shaped temperature profile with two peaks and one valley in the middle gradually forms when the defocus distance changes from -1.5 mm to -3.5 mm, as shown in Figure 15. With the increase in the defocus distance, the time between the two temperature peaks increased, and the value of the temperature peak decreased. The laser scanning speed was constant; hence, the increase in time was mainly caused by the increase in the laser spot distance with the increase in the defocus distance. The larger the absolute defocus distance, the more distinct the shape of the three Gaussian beams. As the three-beam laser moves forward, point P is first heated up by the center of one Gaussian beam, followed by the middle point of the remaining two beams in succession. However, between these two points, there is a relatively low energy intensity point at the center of the three laser spots, resulting in the valley point in the M-shaped temperature profile.

The top, front, and side views of the molten pool at different defocus distances with laser power of 1300 W, scanning speed of 6 mm/s, and wire feeding rate of 20.5 mm/s ($E_L = 51.6, 68.1, 86.7, 119.1$ J/mm^2 and $D_{VL} = 1.72$ mm^3/mm in the process map in Figure 13) are shown in Figure 16. The molten pool edge is formed by an isothermal boundary at the melting point of stainless steel #304 (1400 ℃). At $H = -3.5$ mm, the energy is mainly concentrated at the center of each beam, and the increase in the absolute defocus distance increases the radius (R_1) and the laser spot distance ($2R_2$) of each beam (Figure 12). Hence, the clad zone temperature, especially at the center of the three beams, considerably decreases (Figure 15). Owing to the insufficient heat intensity and temperature, which was lower than the melting point, the material at the bottom of the clad was unmelted, and the molten pool was not formed (Figure 16(a)). The wire

touched the bottom of the molten pool because the heat was insufficient to melt the wire in time or even move out of the center of the three laser beams. As a result, a fragmented and warped clad was formed, as shown in region 5 in the process map (Figure 13).

At $H = -2.5$ mm and $H = -1.5$ mm, the energy intensity applied to the molten pool increases (Figure 12), causing higher temperature, longer solidification time, and faster convection. Thus, complete molten pools with dilution areas are formed, as shown in Figure 16(b) and (c). The molten pool has sufficient energy to timely melt the wire. The wire is easily maintained and continuously moved in the molten pool. The foregoing well conforms with region 3 in the process map where smooth cladding is mainly generated at defocus distances of -2.5 and -1.5 mm (Figure 13). A valley-shaped molten pool with a deeper melting depth caused by the higher energy intensity and temperature at the center of the cladding zone is formed when the defocus distance is -1.5 mm; this differs from that generated when the defocus distance is -2.5 mm. The width of the molten pool mainly depends on the laser beam size. As the beam size (including that of the three beams) and laser spot distance increase, a wider and flat molten pool is produced at a defocus distance of -2.5 mm.

When $H = -0.5$, the beam size sharply decreases and the energy intensity considerably increases. The temperature at the center of the molten pool reaches the boiling point (2827 ℃) because of the high energy concentration (Figure 15). Under these conditions, the wire can overheat and form into drops before melting into the molten pool. As shown in region 1 in the process map (Figure 13), dripping clad is caused by the excessive energy concentration.


Figure 17 Comparison between predicted and measured temperatures: **a** $H = -1.5$ mm and **b** $H = -2.5$ mm

Ji et al. Chin. J. Mech. Eng. (2021) 34:45

Page 14 of 22

Figure 18 Comparison of cross-sections of deposited material between numerical simulation and experimental results at **a** $H = -2.5$ mm and **b** $H = -1.5$ mm

Figure 19 Comparisons between cross-sections of numerical simulation and experimental clad geometry: width, height, depth, and dilution

In summary, a high defocus distance is not sufficient to generate a molten pool, whereas a low defocus distance can lead to overheating. By simulating the formation of the molten pool at different defocus distances, the generation of a molten pool leading to a smooth cladding layer is observed when the defocus distance is between -1.5 and -2.5 mm.

5.4 Temperature Field and Clad Geometry Validation

The temperature cycle in the numerical simulation was verified by experimental measurements. The measured and computed temperature values during the cladding process at defocus distances of -1.5 and -2.5 mm with the laser power, scanning speed, and wire feeding speed of 1300 W, 6 mm/s, and 20.5 mm/s, respectively, were compared, as shown in Figure 17. The test location of the infrared thermometer was the top point of the center width and mid-length of clad to measure the temperature. The experimentally measured and numerically predicted temperature values exceeding 800 °C (test range of infrared thermometer: 800–3000 °C) at different defocus distances were found to well agree.

The comparison between the experimental micrograph transverse cross-sections (right) and simulated cross-sections (left) of the cladding layer produced at defocus distances of -2.5 and -1.5 mm with the laser power of 1300 W, scanning speed of 6 mm/s, and wire feeding speed of 20.5 mm/s, is shown in Figure 18. The molten pool edge is denoted by the isothermal boundary of the melting point of stainless steel #304 (1400 °C) when the cladding depth and heat cycle reach their maximum values. The melting depth is determined by finding the
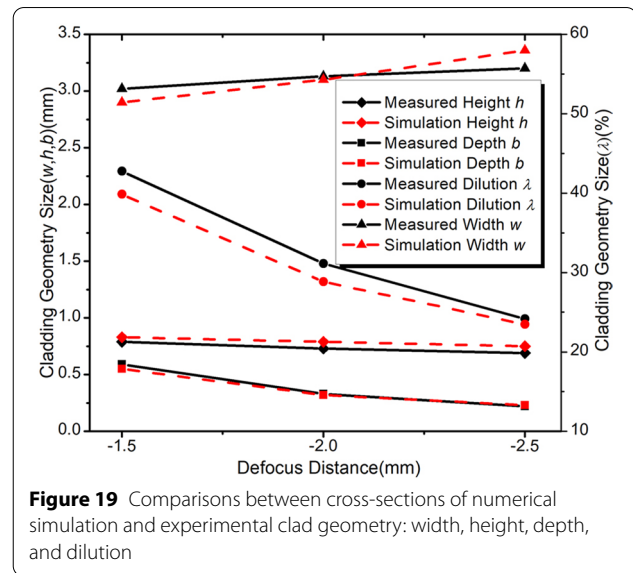
position of the melting temperature at the maximum heat interaction time from the simulated isotherms. The melting zone and the unmelted substrate on the left are represented by the gray and red zones, respectively. The melting boundary of the experimental micrographs could be clearly recognized on the right side. The shape of the simulated molten pool well agrees with the experimental results. At $H = -1.5$ mm, a valley-shaped bond caused by the concentration of the three beams is formed. At $H = -2.5$ m, a flat-bottomed molten pool with low dilution is formed as the laser spot distance increases. As shown in Figures 17 and 18, the experimentally measured and numerically predicted temperatures and heat distributions during the laser cladding process well agree.

The effects of the defocus distance on the geometrical characteristics of the cladding layer with the laser power of 1300 W, scanning speed of 6 mm/s, and wire feeding speed of 20.5 mm/s ($E_L = 68.1$, 76.3, 86.7 J/mm^2; $D_{VL} = 1.72$ mm^3/mm in the process map in Figure 13) are shown in Figure 19. When the defocus distance increases from -1.5 to -2.5 mm, the clad width increases, whereas the height and dilution decrease. The clad dimensions are mainly determined by the laser power, scanning speed, wire feeding speed, and defocus distance. When the other parameters are constant, the defocus distance affects the geometrical characteristics of the clad with the variation in the energy intensity and beam size (including that of the three beams) and laser spot distance. The width of the cladding layer mainly depends on the beam size including each laser spot size ($2R_1$) and laser spot distance ($2R_2$). Due to the larger beam size at $H = -2.5$ mm, a wider molten pool and larger cladding layer width are

Ji *et al. Chin. J. Mech. Eng.* (2021) 34:45

Page 15 of 22
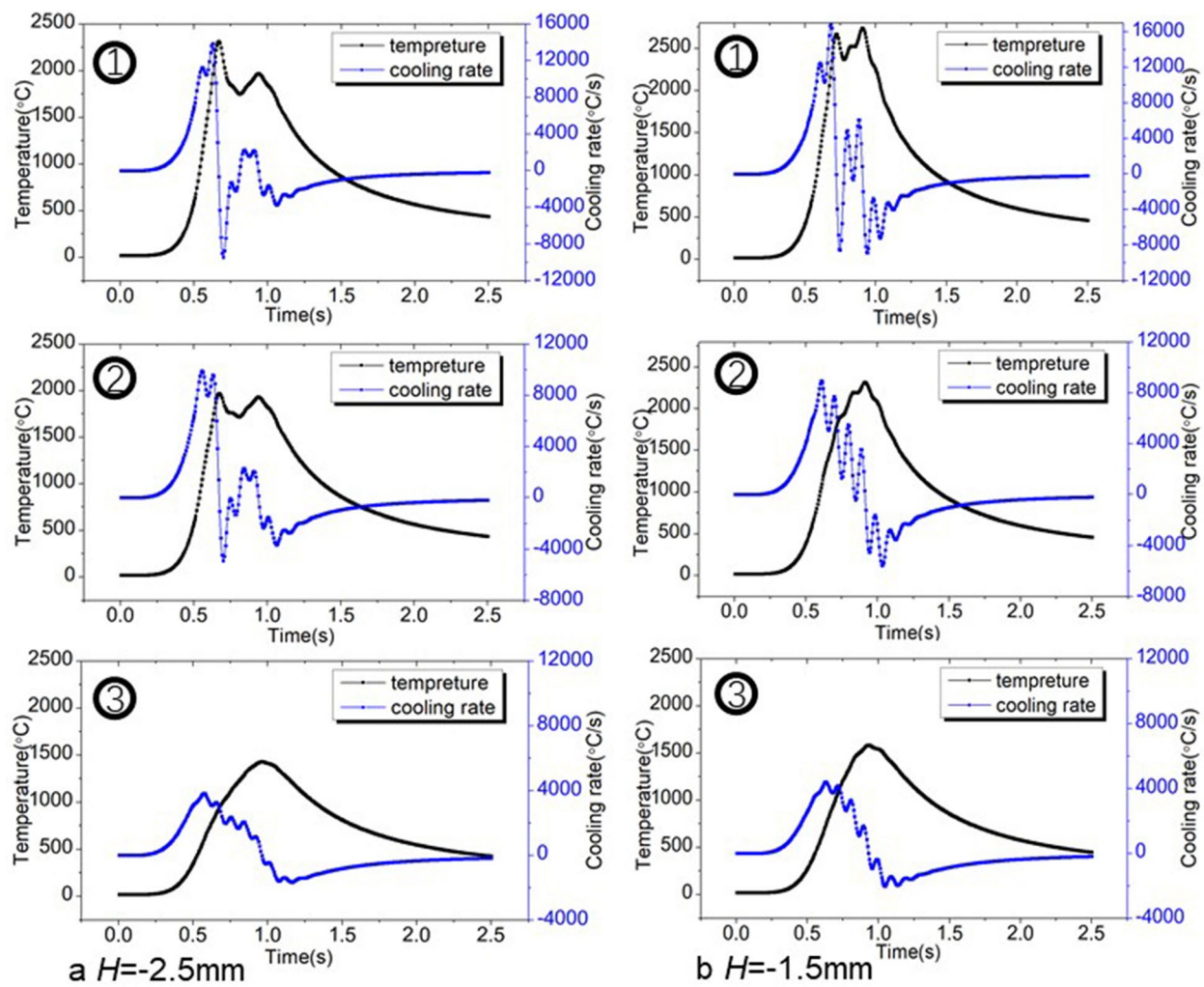
Figure 20 Temperature histories and cooling rate evolutions: **a** $H = -2.5$ mm and **b** $H = -1.5$ mm; ① top of clad, ② center of clad, and ③ bottom of clad

generated than those at $H = -1.5$ mm (Figure 12). The cladding depth and dilution are significantly decreased by the lower energy intensity and larger laser spot distance with the increase in the defocus distance, as shown in Figure 19. With the scanning velocity and wire feeding speed fixed, the deposition volume per unit length and cross-sectional area of the clad remain constant. With the other parameters fixed, the height of the cladding layer decreases with the increase in the defocus distance.

The width, height, and melting depth of the simulated cladding layer and experimental measurements at different defocus distances with the laser power, scanning speed, and wire feeding speed of 1300 W, 6 mm/s, and 20.5 mm/s, respectively (Figure 18), are compared in Figure 19. The maximum deviations between the experimental measurements and numerical simulation results

for the cladding layer width, cladding layer height, melting depth, and dilution are 5%, 8%, 7%, and 7%, respectively. Therefore, a rational and acceptable deviation from the experimental measurements was generated by the thermal model, and the simulated results were consistent with the experimental measurements.

5.5 Microstructure of Clad
The temperature and cooling rate (ε) evolutions at the top, middle, and bottom of the clad (clad zones 1–3 in Figure 18, respectively) at $H = -2.5$ and -1.5 mm are shown in Figure 20. An M-shaped temperature profile with two peaks and one valley is formed at clad zones 1 and 2, respectively, at a defocus distance of $H = -2.5$ mm, as shown in Figure 20(a). There is a short cooling time in the hollow zone at the center of the three

Ji *et al. Chin. J. Mech. Eng.*   (2021) 34:45

Page 16 of 22
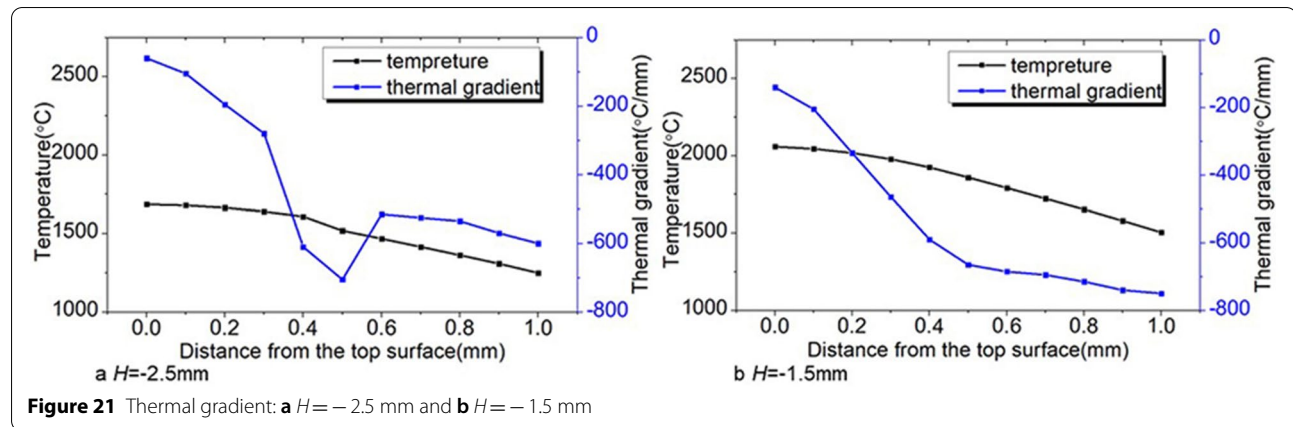
Figure 21 Thermal gradient: **a** $H=-2.5$ mm and **b** $H=-1.5$ mm
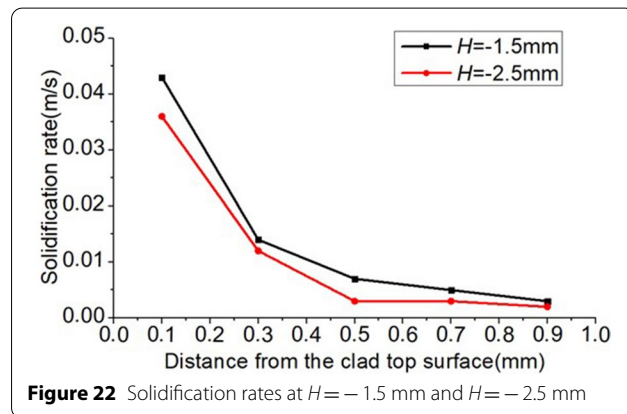
Figure 22 Solidification rates at $H=-1.5$ mm and $H=-2.5$ mm

beams in clad zones 1 and 2, and solidification occurs starting from the second peak in the temperature profile. One peak temperature profile was formed, and solidification started from the peak point in clad zone 3. The maximum cooling rate time point is at 1.06 s. The closer the clad to the heat source, the higher the cooling rate (ε); at the bottom of the clad zone, the cooling rate considerably decreased. The temperature distribution and thermal gradient (G) from the top to the bottom of the clad at the maximum cooling rate time point are shown in Figure 21(b).

The temperature histories and cooling rate (ε) evolutions at $H=-1.5$ mm are shown in Figure 20(b). An M-shaped temperature profile with two peaks and one valley is formed in clad zone 1, whereas only one peak is formed in clad zones 2 and 3. The maximum cooling rate time point is at 1.03 s. The closer the clad to the heat source, the higher the cooling rate (ε). The temperature distribution and thermal gradient from the top to the bottom of the clad at the maximum cooling rate point are shown in Figure 21(b). The temperature decreased along the clad depth direction from top to bottom, whereas the thermal gradient increased. As the concentration of

the laser spots decreased, significant temperature fluctuations at a defocus distance of -2.5 mm were not observed. The largest thermal gradient was observed at the bottom of the clad.

The microstructure characteristics in the clad were affected by the solidification rate in the molten pool. Finer grains are generated at a higher solidification rate, which is determined by the cooling rate and thermal gradient [34]:

$$R = \frac{\varepsilon}{G}, \tag{15}$$

where R is the solidification rate, ε is the cooling rate, and G is the thermal gradient.

The clad microstructures at $H=-1.5$ and -2.5 mm at clad zones 1–3 (Figure 18), are shown in Figure 22; the microstructure characteristics at these defocus distances have identical change trends. Fine dendrite structures (Figure 23(a1) and (b1)) are generated at the top of the clad (zone 1) owing to the high solidification rate (Figure 22). A finer grain size caused by a higher solidification rate is generated when the defocus distance is -1.5 mm at the top of the clad (zone 1) compared with that when the defocus distance is -2.5 mm. At the bottom of the clad (zone 3), the heat transfer is mainly caused by the thermal conductivity of the substrate. In this zone, large columnar structures resulting from the lower solidification rate are predominant. When the defocus distances are -1.5 and -2.5 mm, no distinct difference among the grain sizes is observed at the bottom of the clad because the solidification rates of the grains are virtually the same. The uniform cellular crystals at the middle of the clad (zone 2 in Figure 23(a2) and (b2)) are investigated. When the defocus distance is -1.5 mm, a finer grain size is found at the middle of clad due to the larger solidification rate than that when the defocus distance is -2.5 mm.
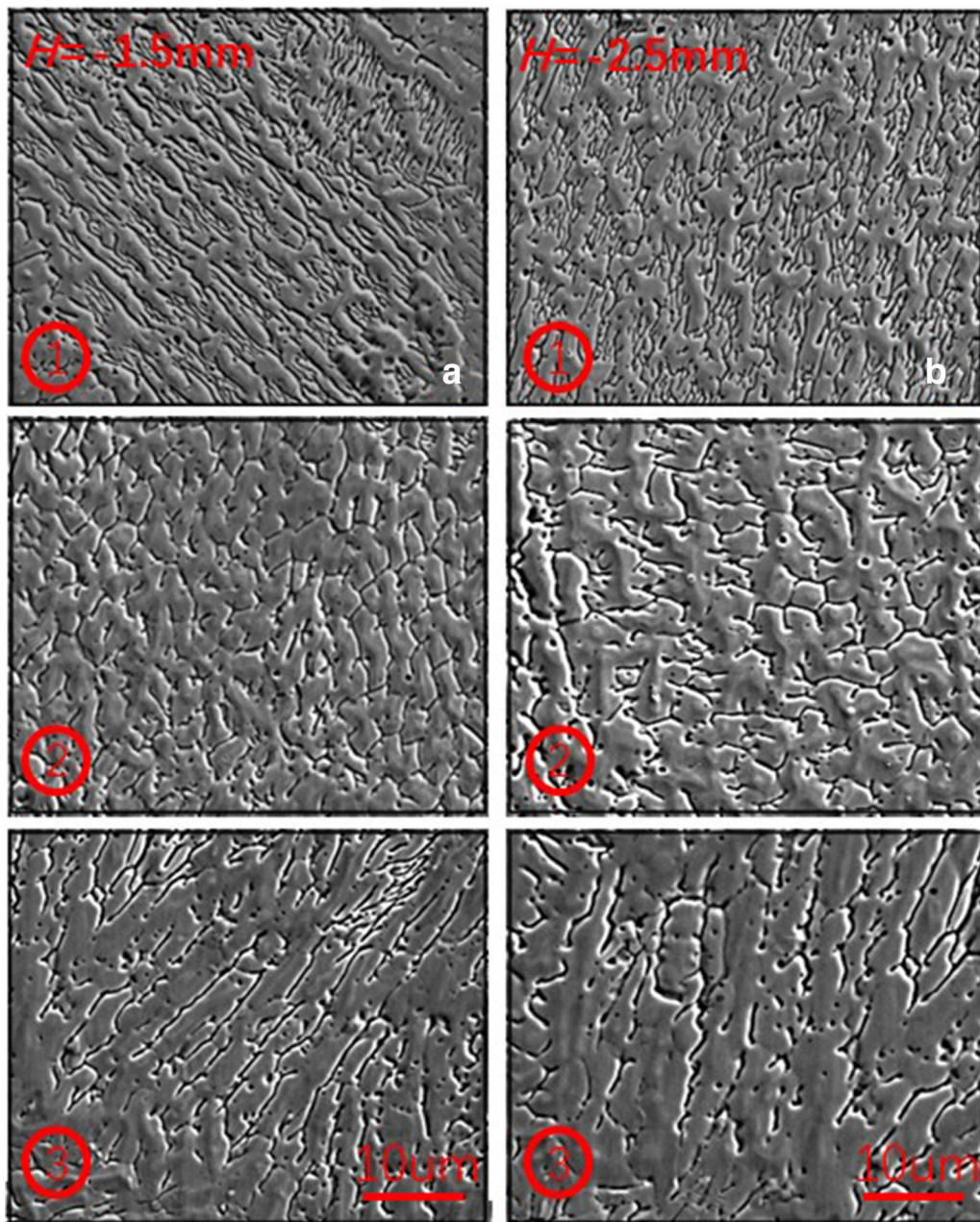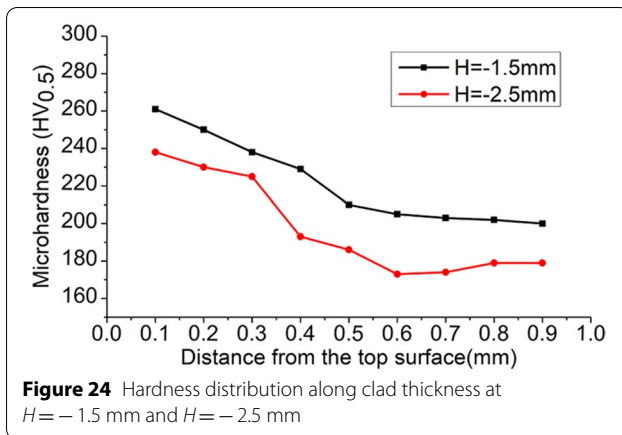
Figure 23 Microstructure at areas 1, 2, and 3 when defocus distances are **a** − 1.5 mm and **b** − 2.5 mm

The finer grains improve the hardness of the material. The microhardness of the cross-sections of the clad at defocus distances of − 2.5 and − 1.5 mm is shown in Figure 24. The testing points were chosen from the top to the bottom of the clad along the centerline of the cross-section. Higher hardness was observed at the top and center of the clad. The hardness value at the bottom of the clad was low because of the coarse grain and high dilution at this location. Contributed by the higher solidification rate, the clad hardness at the defocus distance of − 1.5 mm is 20 $HV_{0.5}$ higher than that at the defocus distance of − 2.5 mm on average.

5.6 Influences of Defocus Distance with Various Parameter Combinations on Clad Geometry

The effects of defocus distance with various parameter combinations, including laser power, scanning speed, and

Ji *et al. Chin. J. Mech. Eng.*   (2021) 34:45

Page 18 of 22

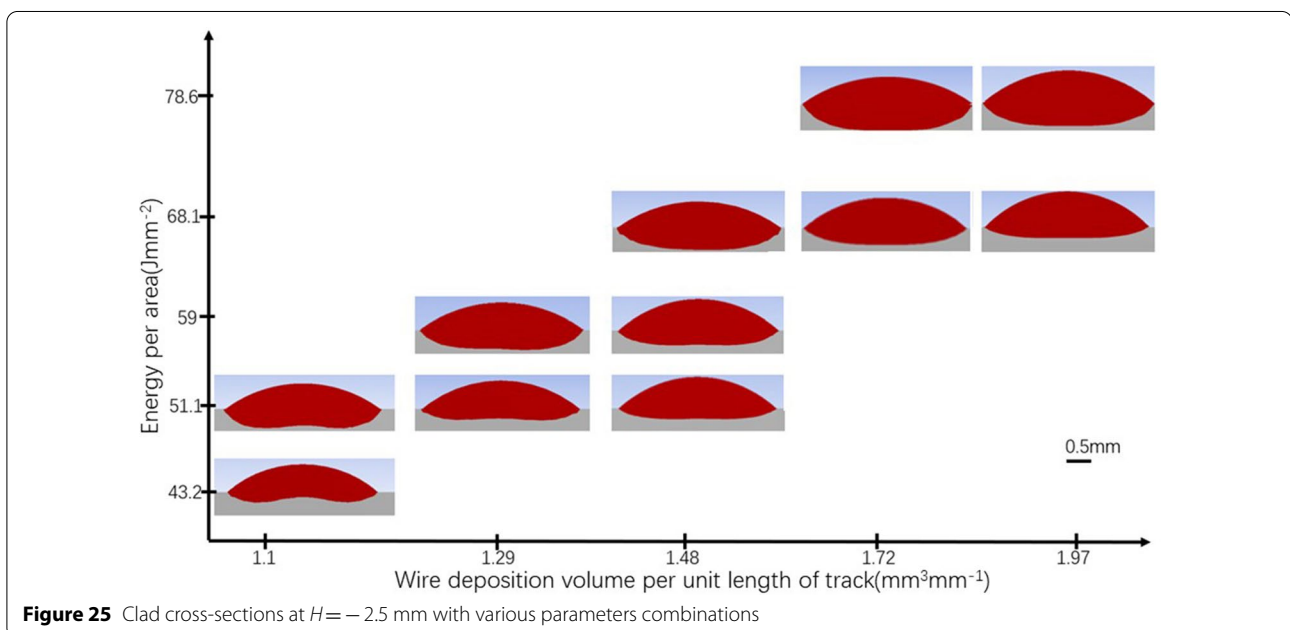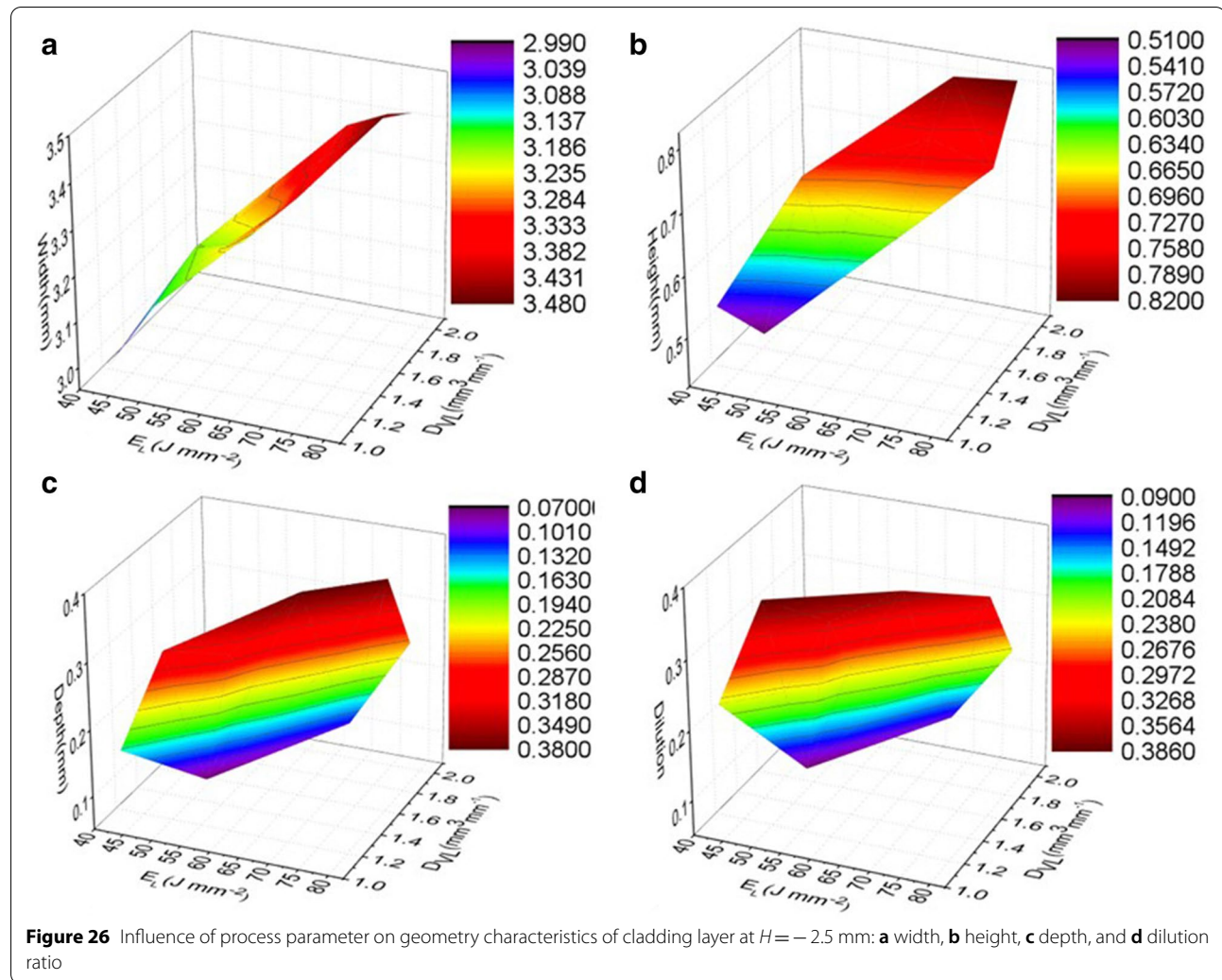**Figure 24** Hardness distribution along clad thickness at $H = -1.5$ mm and $H = -2.5$ mm

wire feeding speed, on the geometry characteristics were explored through the formulated FE model. Numerical studies were performed based on the parameter combinations causing smooth cladding in the process map (region 3 in Figure 13). The simulation results of the effects of the defocus distance with various parameter combinations on the clad geometry are presented in Figures 25, 26, 27, 28. The energy per unit area on the *y*-axis is determined by dividing the laser power by the scanning speed and three-beam laser dimensions (Eq. (13)). The wire deposition volume per unit length on the *x*-axis is a function of the wire feeding speed, cross-sectional area of the wire, and scanning speed (Eq. (14)).

The clad width increases with the energy per unit area. However, it only increases slightly with the deposition

volume per unit length, provided that other factors remain constant, as shown in Figures 26(a) and 28(a). Increasing the laser power and/or decreasing the scanning speed increased the energy per unit area. The cladding layer width increased rapidly at low energy per unit area. At high energy per unit area, the width approximated the outer diameter of the three laser spots $(2R_1 + 2R_2)$; thereafter, it only increased marginally. The foregoing shows that the laser beam dimensions (including the three beams) and beam spot distance are the approximate the limit of the width of the achievable cladding layer. As for the increase in the wire deposition volume, the width may be slightly increased because of the gravity effect of the increase in the molten pool volume. A wider width at a defocus distance of -2.5 mm is found compared with that at $H = -1.5$ mm with the same combinations of energy per unit area and wire deposition volume per unit length. This is attributed to the longer beam spot distance and larger size of the single beam.

The height of the cladding layer significantly increases with the deposition volume per unit length but slightly decreases with the increase in energy per unit area, provided, other factors remain constant, as shown in Figures 26(b) and 28(b). Increasing the wire feeding speed and/or decreasing the scanning speed increased the wire deposition volume per unit length. This resulted in an increase in the cross-sectional area of the clad. Thus, the clad height considerably increased with a slight increase in width. The increase in energy per unit area resulted in higher temperature and longer solidification time, providing the molten pool sufficient time to release

Figure 25 Clad cross-sections at $H = -2.5$ mm with various parameters combinations

Ji *et al. Chin. J. Mech. Eng.*   (2021) 34:45

Page 19 of 22

Figure 26 Influence of process parameter on geometry characteristics of cladding layer at $H = -2.5$ mm: **a** width, **b** height, **c** depth, and **d** dilution ratio

its surface tension. As a result, the clad height slightly decreased. A lower height was obtained when the defocus distance was -2.5 mm compared with that when $H = -1.5$ mm. This resulted from a wider clad width at the same combination of energy per unit area and wire deposition volume per unit length.

As shown in Figures 26(d) and 28(d), the dilution increases by increasing the energy per unit area but decreases by increasing the wire deposition volume per unit length, when the other parameters are fixed. The dilution depends on the volumes of the molten substrate and feeding wire. With the increase in the laser power, the volume of the molten substrate increased because of the increase in the energy input. This also accelerated the vigorous movement of the molten pool and mixing of the substrate with the cladding layer, leading to greater melting depth and dilution. With the increase in the wire feeding speed, the energy reaching the substrate was considerably reduced by the increase in the wire deposition

volume. As a result, low melting depth and dilution were generated. With the increase in the scanning speed, the wire deposition volume per unit length and energy per unit area both decreased. A smaller cladding was generated by the reduced wire deposition volume. Furthermore, the decreased energy per unit area reduced the melting depth of the substrate. However, influence of this energy on the melting depth compared with that on the clad volume was less significant. Therefore, the dilution increased with the scanning speed. Shorter laser spot distances and smaller beam sizes at a defocus distance of -1.5 mm resulted in a higher energy concentration at the center of the molten pool. As shown in Figures 25 and 27, a valley-shaped bottom and a relatively flat bottom are observed, when the defocus distances are -1.5 and -2.5 mm, respectively. For each parameter combination, higher melting depths and dilutions are produced at $H = -1.5$ mm compared with those at $H = -2.5$ mm. With the combination of low energy per unit area and
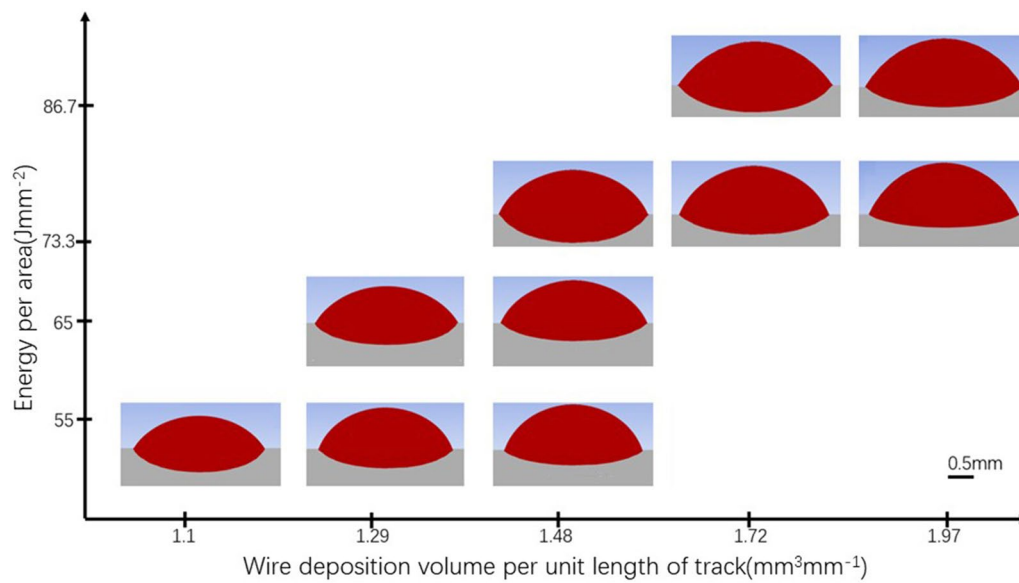
Figure 27 Clad cross-sections at $H = -1.5$ mm with various parameter combinations

relatively high wire deposition volume per unit length, cladding layers with dilution ratios of 9% and 13.8% at defocus distances of -2.5 and -1.5 mm were obtained, respectively.

6 Conclusions

In this study, numerical and experimental methods were utilized to investigate and calculate the thermal gradient, temperature history, molten pool shape, and clad geometry of a three-beam laser internal wire feeding cladding at different defocus distances. A process map was developed to indicate the process characteristics at different defocus distances to determine the parameter combination yielding a smooth clad. A 3D transient thermal model was formulated based on the calculation results of TracePro of the transmission characteristics of the three-beam laser. Several conclusions are drawn from this study.

(1) The TracePro calculation results show that with the increase in the absolute defocus distance, the diameter of each laser beam ($2R_1$) and laser spot distance ($2R_2$) increase, whereas the heat intensity (q_m) considerably decreases.

(2) The process map indicates that most of the smooth cladding layers are obtained when the defocus distance is from -1.5 to -2.5. When the defocus distance is less than -1.5 mm, wire dripping mainly occurs; when it reaches -3.5 mm, wire stubbing is predominant. This is consistent with the molten pool simulations in which overheating occurs at a low defocus distance, whereas the energy intensity

is extremely low to generate the molten pool at a high defocus distance.

(3) The numerical results show that the various energy intensities and laser spot distances applied to the molten pool at different defocus distances cause the different temperature evolutions and molten pool shapes in the cladding process. When the defocus distance is from -1.5 to -2.5 mm, a heart-shaped molten pool with an M-shaped temperature profile at the center of the clad is formed. A molten pool with a flat bottom and low melting depth is generated when the defocus distance is -2.5 mm. When the defocus distance -1.5 mm, a molten pool with a valley-shaped bond and high melting depth is obtained.

(4) The microstructure and hardness are affected by the defocus distance. The finer grains and higher hardness are investigated because of the higher solidification rate at a defocus distance of -1.5 mm compared with that at -2.5 mm.

(5) The clad geometry is affected by the defocus distance. The height and dilution of the clad decrease, whereas the width increases with the increase in the absolute defocus distance. The effects of the defocus distance with various parameter combinations on the geometrical characteristics were explored through the formulated FE model.

(6) The temperature evolutions were validated by experimental measurements. The simulated clad geometries and experimental measurements were compared and found to well agree. This indicated

Ji *et al. Chin. J. Mech. Eng.*   (2021) 34:45

Page 21 of 22
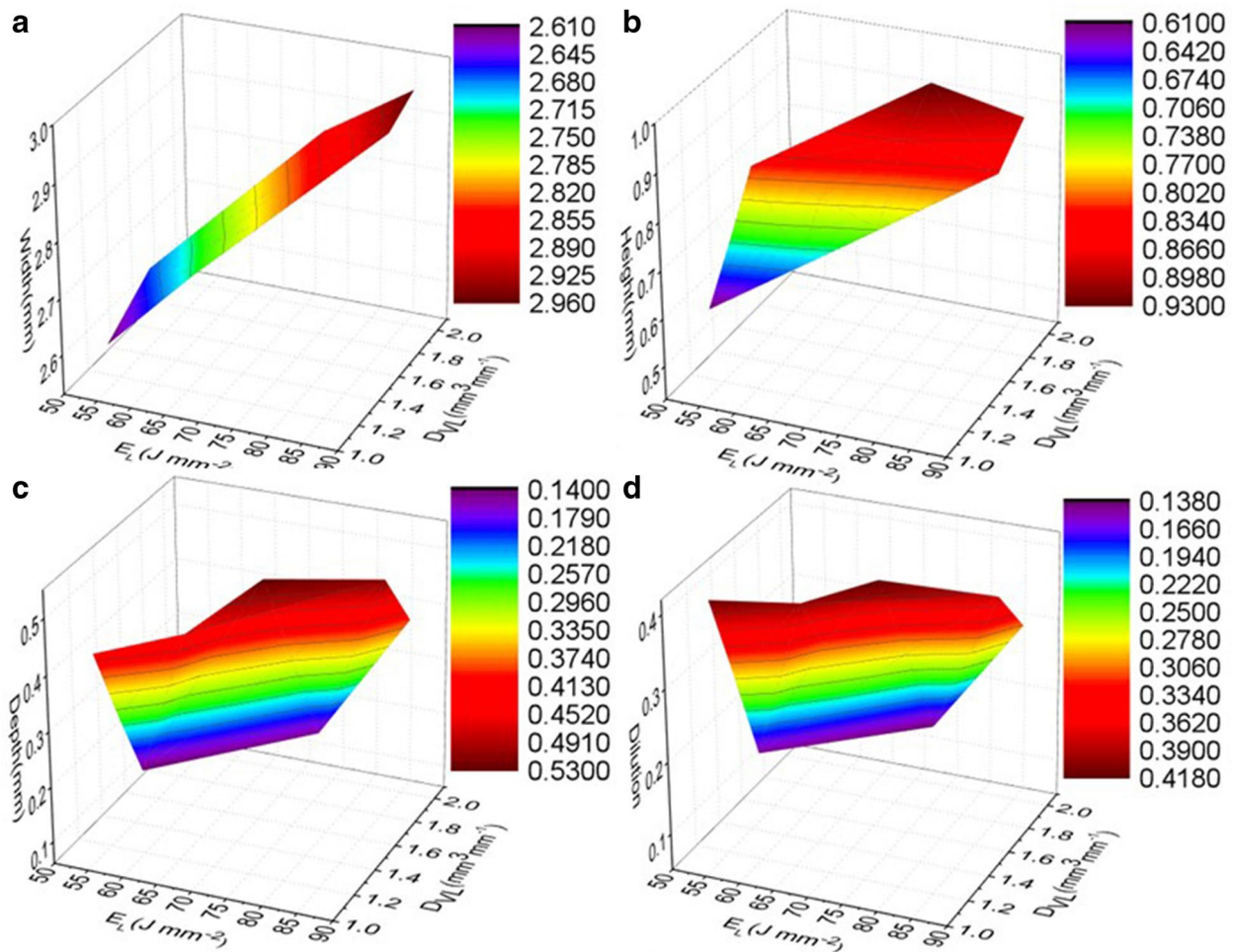
Figure 28 Influence of process parameters on geometrical characteristics of cladding layer at $H = -1.5$ mm: **a** width, **b** height, **c** depth, and **d** dilution ratio

that the formulated model can be utilized to predict the thermal cycles and clad geometry in the laser cladding process.

Authors' Contributions
SJ was in charge of the whole trial; SJ and FL wrote the manuscript; TS, SS and GF assisted with sampling and laboratory analyses. All authors read and approved the final manuscript.

Authors' Information
Shaoshan Ji, born in 1983, is currently a PhD candidate at *School of Mechanical and Electrical Engineering, Soochow University, China*. He received his master's degree from *Soochow University, China*, in 2013. His research interests include laser cladding and the wire-feeding laser metal deposition process.

Fan Liu, born in 1984, is currently a PhD candidate at *School of Mechanical and Electrical Engineering, Soochow University, China*. She received her master's degree from *Soochow University, China*, in 2013. Her research interests include laser cladding and the wire-feeding laser metal deposition process.

Tuo Shi, born in 1984, is currently an associate professor *at the School of Optoelectronic Science and Engineering*, *Soochow University, China*. His research interests include laser additive manufacturing and intelligent control in the laser metal deposition process.

Geyan Fu, born in 1959, is currently a professor at School of *Mechanical and Electrical Engineering, Soochow University, China*. Her research interests include laser cladding and the wire-feeding laser metal deposition process.

Shihong Shi, born in 1956, is currently a professor at *School of Mechanical and Electrical Engineering, Soochow University, China*. His main research interests include laser cladding, laser additive manufacturing, and optical system development.

Ji *et al. Chin. J. Mech. Eng.* (2021) 34:45

Page 22 of 22

Author Details
[1] School of Mechanical and Electrical Engineering, Soochow University, Suzhou 215000, China. [2] School of Optoelectronic Science and Engineering, Soochow University, Suzhou 215000, China.

References
[1] E Toyserkani, S Corbin, A Khajepour. *Laser cladding*. CRC, Canada. 2005.
[2] W F Wang, M C Wang, Z Jie, et al. Research on the microstructure and wear resistance of titanium alloy structural members repaired by laser cladding. *Opt. Lasers Eng.*, 2008, 46: 810-816.
[3] A J Pinkerton. Advances in the modeling of laser direct metal deposition. *Journal of Laser Applications*, 2015, 27: S15001.
[4] Ul Waheed, Haq Syed, Lin Li. Effects of wire feeding direction and location in multiple layer diode laser direct metal deposition. *Applied Surface Science*, 2005, 248: 518-524.
[5] J Kim, Y Peng. Plunging method for Nd: YAG laser cladding with wire feeding. *Opt. Lasers Eng.*, 2000, 33: 299-309.
[6] A S Salminen, V P Kujanpaa, T J Moisio. Interactions between laser beam and filler metal. *Weld J.*, 1996, 75(1): 9-13.
[7] X D Zhang, W Z Chen, Y Q Shuang, et al. Coaxial hybrid CO2 laser-MIG welding system and its application in welding of aluminum. *Appl. Laser*, 2005, 25(22): 1-3.
[8] G Y Fu, S S Ji, S H Shi. A device of coaxial wire feeding through beams for laser cladding: China, CN201610075735. 2017-09-05.
[9] S S Ji, F Liu, G Y Fu. New forming method of coaxial wire feeding inside three beams laser cladding. *Surface Technology*, 2019(4): 287-289. (in Chinese)
[10] H Gu, L Li. Computational fluid dynamic simulation of gravity and pressure effects in laser metal deposition for potential additive manufacturing in space. *International Journal of Heat and Mass Transfer*, 2019, 140: 51-61.
[11] J T Hoffman, D F DeLange, B Pathiraj, et al. FEM modeling and experimental verification for dilution control in laser cladding. *J. Mater. Process. Technol.*, 2011, 211: 187-196.
[12] E A Hochmann, I Salehinia. How convection on the substrate affects the thermal history of the build in direct laser deposition—finite element analysis. *The International Journal of Advanced Manufacturing Technology*, 2018, 96: 3471-3480.
[13] W Ya, B. Pathiraj, S J Liu. 2D modelling of clad geometry and resulting thermal cycles during laser cladding. *Journal of Materials Processing Technology*, 2016, 230: 217-232.
[14] P Farahmand, R Kovacevic. An experimental–numerical investigation of heat distribution and stress field in single-and multi-track laser cladding by a high-power direct diode laser. *Optics & Laser Technology*, 2014, 63: 154-168.
[15] M Z Hao, Y W Sun. A FEM model for simulating temperature field in coaxial laser cladding of TI6AL4V alloy using an inverse modeling approach. *International Journal of Heat and Mass Transfer*, 2013, 64: 352-360.
[16] S Kumar, V Sharma, A K S Choudhary, et al. Determination of layer thickness in direct metal deposition using dimensional analysis. *Int. J. Adv. Manuf. Technol.*, 2013, 67(9-12): 2681-2687.
[17] M Ansari, R S Razavi, M Barekat. An empirical-statistical model for coaxial laser cladding of NiCrAlY powder on Inconel 738 superalloy. *Optics and Laser Technology*, 2016, 86: 136-144.
[18] M Nabhani, R S Razavi, M Barekat. An empirical-statistical model for laser cladding of Ti-6Al-4V powder on Ti-6Al-4V substrate. *Optics and Laser Technology*, 2018, 100: 265-271.
[19] S H Wang, L D Zhu, J Y H Fuh, et al. Multi-physics modeling and Gaussian process regression analysis of cladding track geometry for direct energy deposition. *Optics and Lasers in Engineering*, 2020, 127: 105950.
[20] T E Abioye, J Folkes, A T Clare. A parametric study of Inconel 625 wire laser deposition. *Journal of Materials Processing Technology*, 2013, 213: 2145-2151.
[21] E Toyserkani, A Khajepour, S Corbin. Three-dimensional finite element modeling of laser cladding by powder injection: effects of powder feed rate and travel speed on the process. *J. Laser Appl.*, 2003, 15 (3): 153-160.
[22] I Tabernero, A Lamikiz, S Martinez, et al. Geometric modelling of added layers by coaxial laser cladding. *Phys. Proc.*, 2012, 39: 913-920.
[23] H M Liu, X P Qin. Geometry modeling of single track cladding deposited by high power diode laser with rectangular beam spot. *Optics and Lasers in Engineering*, 2018, 100: 38-46.
[24] A Riquelme, P Rodrigo, M D Escalera-Rodriguez, et al. Analysis and optimization of process parameters in Al–SiCp laser cladding. *Opt. Lasers Eng.*, 2016, 78: 165-173.
[25] G X Zhu, A F Zhang, D C Li. Effect of process parameters on surface smoothness in laser cladding. *Chin. J. Lasers*, 2010, 37: 296-301. (in Chinese)
[26] W Gao, S Zhao, F Liu, et al. Effects of defocus plane on laser cladding of Fe-based alloy powder. *Surf. Coat. Technol.*, 2014, 248: 54-62.
[27] J J Shi, P Zhu, G Y Fu, et al. Geometry characteristics modeling and process optimization in coaxial laser inside wire cladding. *Optics and Laser Technology*, 2018, 101: 341-348.
[28] A Suarez, J Amado, M Tobar, et al. Study of residual stresses generated inside laser cladded plates using FEM and diffraction of synchrotron radiation. *Surf. Coat Tech.*, 2010, 204: 1983-1988.
[29] M Alimardani. *Multi-physics analysis of laser solid free form fabrication*. Canada: University of Waterloo, 2009.
[30] M Labudovic, D Hu, R Kovacevic. A three dimensional model for direct laser metal powder deposition and rapid prototyping. *J. Mater. Sci.*, 2003, 38: 35-49.
[31] F Liu, S S Ji, G Y Fu. The influence of process parameters on geometry characteristics by three beams laser cladding. *Journal of Mechanical Engineering*, 2020, 15: 227-237. (in Chinese)
[32] N Chekir, Y Tian, R Gauvin, et al. Laser wire deposition of thick Ti-6Al-4V buildups: Heat transfer model, microstructure, and mechanical properties evaluations. *Metallurgical and Materials Transactions*, 2018, 49: 6490-6508.
[33] Z G Nie, G Wang, D James, et al. Experimental study and modeling of H13 steel deposition using laser hot-wire additive manufacturing. *Journal of Materials Processing Technology*, 2016, 235: 171-186.
[34] J Dantzig, M Rappaz. *Solidification methods microstructure and modeling*. EPFL Press, 2009.